Conformal Mechanics of Serpentine Meshes for Millimeter-Scale Neural Probes.

Sagidolla Batay[1], Yulin Zhou[1], Priyan V. Pathirana[2], John P. Seymour[2,3,4,5], and Raudel Avila[1,3,6,7,*]

[1]Department of Mechanical Engineering, Rice University, Houston, Texas, 77005
[2]Department of Electrical & Computer Engineering, Rice University, Houston, Texas, 77005
[3]Rice Neuroengineering Initiative, Rice University, Houston, Texas, 77005
[4]Vivian L. Smith Department of Neurosurgery, McGovern Medical School, University of Texas Health Science Center at Houston, Houston, Texas, 77030
[5]Texas Institute for Restorative Neurotechnologies, University of Texas Health Science Center at Houston, Houston, Texas, 77030
[6]Rice Advanced Materials Institute, Rice University, Houston, Texas, 77005
[7]Digital Health Institute, Rice University, Houston, Texas, 77005

*Corresponding Author: Raudel Avila (ra88@rice.edu)

KEYWORDS
Stretchable neural probes
Serpentine interconnects
Mesh electronics
Conformal mechanics
Finite element analysis

HIGHLIGHTS

1. Topology governs stress localization and yielding in cylindrical neural probe architectures.
2. Rotational compliance reduces peak stress and delays yielding in serpentine interconnects.
3. Conformal wrapping of small-radius cylindrical neural probes is the dominant mechanical loading condition.
4. Interconnection junctions improve connectivity but amplify stress concentrations and accelerate yielding.

ABSTRACT

The mechanical reliability of implantable neural probes depends on their ability to accommodate large deformations during implantation and chronic operation while limiting stress concentrations within conductive interconnects. Despite extensive studies of serpentine interconnects in stretchable electronics, their mechanics under loading conditions relevant to cylindrical neural probes remain poorly understood. This work investigates the mechanics of two stretchable neural interface architectures, Single Serpentine Traces and Interconnected Mesh networks, designed with gold (Au) interconnects encapsulated in polyimide (PI) and embedded within a soft elastomeric substrate. Finite element analysis and experiments are used to characterize their response under stretching, conformal wrapping onto cylindrical neural probes, and bending of the wrapped structure. Deformation in both architectures is accommodated primarily through bending and rotation of the serpentine segments, with localized metal yielding initiating at strains of approximately 5.5–8.25% depending on loading direction and topology. During conformal wrapping onto probes with radii as small as 0.4 mm, the Single Serpentine Traces architecture remains below the Au yield stress, reaching a maximum stress of 145 MPa, whereas the Interconnected Mesh develops localized yielding at interconnection junctions with peak stresses exceeding 215 MPa. Subsequent bending produces only modest stress amplification, although the Interconnected Mesh exhibits approximately twofold greater stress sensitivity than the Single Serpentine Traces. The results demonstrate that rotational compliance governs stress redistribution, while geometric constraints at interconnection junctions control failure initiation. These findings reveal a fundamental tradeoff between electrical connectivity and stress concentrations and provide mechanics guidelines for conformal neural probes and related stretchable bioelectronic systems.

GRAPHICAL ABSTRACT

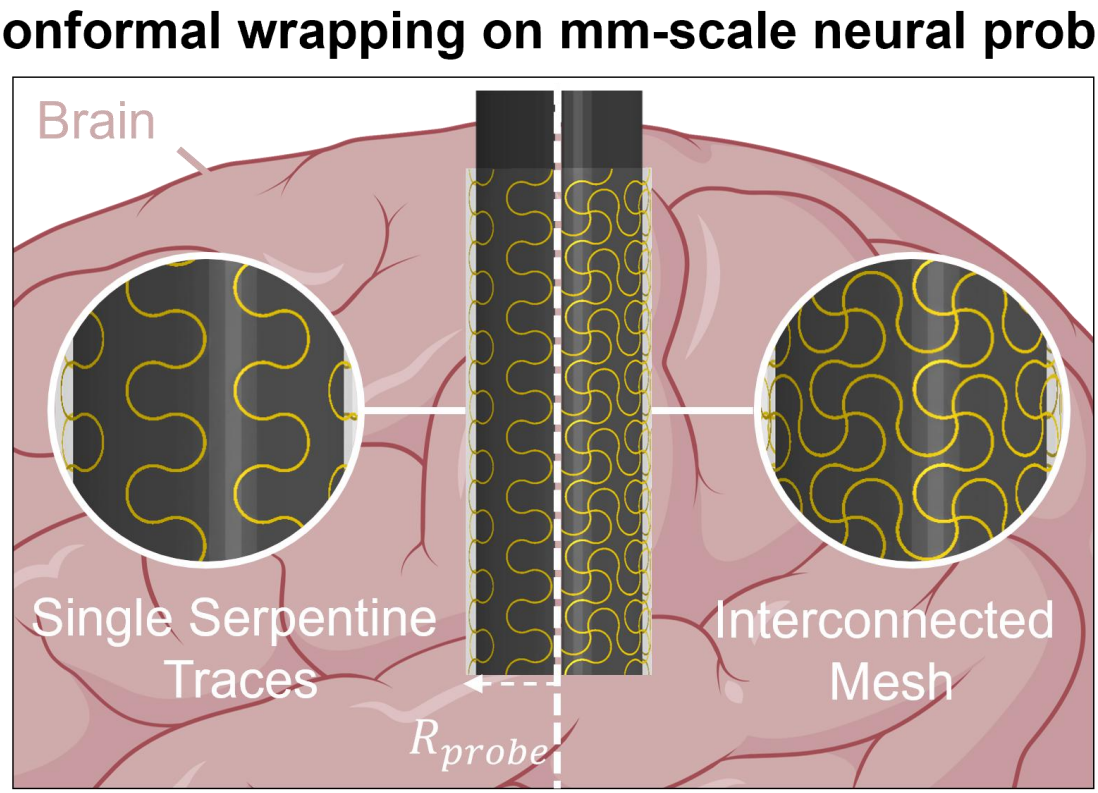

1. INTRODUCTION

Disorders of the nervous system, including stroke, migraine, Alzheimer disease, and Parkinson disease, affect more than 3.4 billion individuals worldwide and impose an economic burden exceeding 800 billion dollars annually in the United States alone (Bazargan-Hejazi et al., 2020; Steinmetz et al., 2024). Advancing the understanding and treatment of these conditions requires neural interfaces capable of recording electrophysiological activity with high spatial and temporal resolution. Recent developments in high-density neural probes have enabled measurements at cellular scales, providing unprecedented access to neural circuit dynamics (Jun et al., 2017). A central challenge in implantable chronic neural interfaces arises from the severe mechanical mismatch between soft neural tissue and conventional probe materials. Brain tissue exhibits a Young modulus in the range of 1 kPa–100 kPa (Sridharan et al., 2013a), whereas silicon shanks possess moduli of 130–188 GPa (Hopcroft et al., 2010) and tungsten microwires exceed 400 GPa (Sridharan et al., 2015). While viable for acute implantation, this mismatch amplifies interfacial stresses generated by vascular pulsation and respiratory-induced micromotion of the brain (Nguyen et al., 2014). The resulting shear deformation at the tissue–probe interface triggers chronic inflammatory responses, including microglial activation and astrocytic encapsulation (Sharon et al., 2021; Savya et al., 2022; Wang et al., 2025a), which progressively increase interfacial impedance and degrade recording quality over time (Salatino et al., 2017; Wang et al., 2025b).

To reduce tissue trauma, clinical depth electrodes commonly adopt cylindrical architectures. Stereoelectroencephalography (SEEG) probes or deep brain stimulators (DBS) typically feature diameters of 0.8–1.37 mm and integrate platinum-iridium macroelectrodes along polymeric shafts for local field potential recording and stimulation (Pothof et al., 2016a; Kullmann et al., 2024). Although these device architectures broaden diagnostic capability, manual assembly necessitates individual routing of discrete electrical conductors imposing fundamental limitations on channel density because of the restricted internal volume available (Pothof et al., 2016a). Flexible thin-film electronics provide an alternative strategy to increase channel density while reducing structural stiffness. Polyimide (PI) and Parylene-C thin films with embedded metallic interconnects enable high-density recording arrays with total thicknesses of 10–50 μm (Park et al., 2015; Liu et al., 2019; Freitas et al., 2022; McGlynn et al., 2022). Further reductions in thickness have been achieved through ultrathin architectures approaching 1 μm, thereby increasing mechanical compliance and reducing bending stiffness by several orders of magnitude (Luan et al., 2017). These planar systems can be conformally wrapped into cylindrical geometries that match the dimensions of clinical SEEG probes (Pothof et al., 2016a; Abrego et al., 2023). However, rolled thin-film neural interfaces rely on nearly inextensible metallic traces and semi-rigid supporting backbones to preserve cylindrical geometry (Pothof et al., 2016a). Consequently, they cannot effectively accommodate the multi-axial deformation associated with brain swelling, vascular pulsation, and chronic tissue motion (Kozai et al., 2015; Sharafkhani et al., 2022a). Repeated deformation under these conditions promotes stress accumulation within the metallic interconnects and accelerates mechanical failure of thin-film electrodes (Schulte et al., 2024).

Serpentine interconnects embedded within elastomeric substrates provide an effective strategy towards mechanically compliant neural interfaces. Elastomeric materials possess elastic moduli comparable to soft tissue (~kilopascals) while simultaneously serving as biocompatible encapsulation layers for implantable electronics (Park et al., 2015; Lacour et al., 2016; Liu et al., 2019). More importantly, serpentine geometries transform axial deformation into distributed bending and rotational modes of the curved segments (Rogers et al., 2010; Zhang et al., 2013a). This geometrical non-linearity suppresses stress concentrations and delays yielding within the conductive films during large deformation. Interconnection topology further governs the rotational compliance and stress redistribution of the network, thereby strongly influencing the localization of stress under multi-axial loading. Suppressing these localized stress concentrations is particularly important because cyclic micromotion can accelerate fatigue and fracture in ultrathin (~nano-micro) metallic interconnects.

While the mechanics of serpentine interconnects under planar stretching are well understood, cylindrical integration introduces additional constraints associated with curvature that can alter stress distributions within the structure. Existing analytical and computational models have established how serpentine geometries accommodate planar deformation through bending and rotation of the curved segments, enabling large elastic stretchability while delaying the onset of yielding (Zhang et al., 2013b; Fan et al., 2016a; Pan et al., 2017a). These studies provide a rigorous understanding of stress localization, stretchability, and buckling under planar loading. However, cylindrical integration introduces fundamentally different deformation modes. Wrapping onto

a cylindrical substrate generates curvature-induced bending across the thickness of the structure, producing simultaneous tensile and compressive stresses while imposing geometric constraints that depend strongly on interconnect topology. Subsequent manipulation of the curved substrate further modifies the stress state through the interaction of bending, curvature, and topology. The extent to which these mechanisms govern stress localization and yielding in conformal neural interfaces remains largely unexplored.

Mechanical modeling of flexible neural probes has primarily focused on probe–tissue interactions and insertion mechanics. Three-dimensional finite element analyses have shown that compliant polymeric probes substantially reduce tissue strains generated by brain micromotion compared with conventional silicon probes (Subbaroyan et al., 2005; Al Abed et al., 2022; Sharafkhani et al., 2022b). Parallel studies have examined insertion mechanics, where finite element and analytical models have established critical buckling thresholds and informed the design of temporary stiffening strategies (Singh et al., 2016). Together, these efforts have provided important design guidelines for minimizing tissue damage and avoiding structural failure during implantation. However, they do not address the mechanics of the conductive interconnect networks themselves. Recent advances in cylindrical and three-dimensional neural probes have further highlighted this gap. Finite element analysis of the rolling-of-soft-electronics (ROSE) probe demonstrated that interconnect strains remain below ~3% during the rolling fabrication process and established scaling relations governing the resulting three-dimensional geometry (Qiang et al., 2025). Other cylindrical neural probe platforms, including wrapped polyimide foils (Fomani et al., 2010; Pothof et al., 2016b), fiber-based probes (Zhang et al., 2025), graphene-polymer probes (Wang et al., 2017), and carbon nanotube fiber probes (Jeon et al., 2024), have focused primarily on electrical characterization, insertion, or electrochemical stability, with little attention given to the mechanics of the interconnects on curved substrates. Even studies incorporating structural simulations, such as the Neurotassel architecture (Guan et al., 2019), have largely considered planar configurations or assembly processes rather than curvature-induced loading of interconnected conductive networks. This limitation is particularly important for miniaturized neural probes, where small radii of curvature (<0.4 mm) can amplify local stresses and govern mechanical reliability.

This work evaluates two stretchable neural probe architectures designed for conformal cylindrical integration: Single Serpentine Traces and Interconnected Mesh networks. The Single Serpentine Traces architecture represents a mechanically compliant topology that accommodates deformation primarily through independent bending and rotational motion of the serpentine arcs (Zhang et al., 2013d,c; Widlund et al., 2014; Fan et al., 2016b; Pan et al., 2017b). In contrast, the Interconnected Mesh architecture introduces orthogonal interconnectivity between adjacent serpentine segments, thereby increasing geometric constraint and modifying stress redistribution during multi-axial deformation (Ma et al., 2016; Sim et al., 2019; Li et al., 2026). Both systems consist of ultrathin Au traces encapsulated within polyimide and embedded in an Ecoflex 00-30 substrate supported by a NuSil-Med-6019 backing layer. Finite element analysis is used to quantify stress evolution and yielding behavior under loading conditions representative of fabrication, deployment, and operation. Experimental optical images of the deformed architectures during stretching and conformal wrapping are used to assess the predicted deformation modes and overall kinematic response. The first loading condition considers uniaxial and biaxial stretching up to 30% strain to evaluate deformation associated with device handling, transfer, mounting, and tissue micromotion during chronic implantation. The second loading condition examines conformal wrapping around poly(dimethylsiloxane) (PDMS) cylindrical substrates with radii of 0.4–0.7 mm, corresponding to clinically relevant neural probe dimensions (Pothof et al., 2016a; Kullmann et al., 2024). The third loading condition investigates bending of the wrapped structures along a 50 mm cylindrical probe subjected to transverse displacement, representing deformation induced by implantation into curved neural structures and chronic in vivo motion. By systematically comparing stress localization, curvature accommodation, and yielding behavior across these loading conditions, this study reveals the mechanics governing conformal serpentine neural interfaces and identifies the geometric mechanisms that suppress stress concentration in cylindrical implantable electronics.

2. MATERIALS AND METHODS

2.1.1 Design and Material Description

Figure 1 summarizes the neural probe architectures, material stack-up, geometric layouts, and fabricated samples. Both designs target conformal cylindrical neural interfaces and differ primarily in interconnect topology. The first architecture consists of Single Serpentine Traces, whereas the second adopts an Interconnected Mesh configuration formed through orthogonal coupling of serpentine networks. The multilayer structure in **Figure 1B** comprises PI encapsulation layers of thickness t_{PI}, ultrathin Au serpentine traces of thickness t_{Au}, an Ecoflex 00-30 substrate of thickness t_E, and a NuSil-Med-6019 (NuSil) backing layer of thickness t_N, resulting in a total device thickness t_D = 25 μm. The Au traces are encapsulated within PI because of its chemical resistance and mechanical durability in implantable electronic systems (Pimenta et al., 2024; Menghani and Avila, 2025). The PI/Au/PI composite is embedded within Ecoflex, whose low modulus and large deformability reduces strain transfer into the metallic interconnects during deformation (Xie et al., 2018; Ye et al., 2020). A NuSil backing layer provides mechanical support, biocompatibility, and fabrication stability while enabling controlled Ecoflex thickness (Russo et al., 2017).

The Single Serpentine Traces architecture in **Figure 1C** consists of eight parallel rows of horseshoe-shaped serpentine interconnects characterized by width $W = 0.01$ mm, offset angle $\theta = 25°$, and arc radius $r = 0.084$ mm. This geometry accommodates deformation primarily through bending and rotational motion of the curved segments. Mechanical evaluation uses square specimens with dimensions $L \times L = 2.6$ mm $\times$ 2.6 mm. The Interconnected Mesh architecture in **Figure 1D** builds upon the same serpentine unit cell but introduces a second serpentine network rotated $90°$about the z-axis. Orthogonal interconnection transforms the structure into an 8×8 coupled serpentine network with enhanced geometric constraint relative to the independent-row configuration of the Single Serpentine Traces design. This topology modifies rotational compliance and stress redistribution during multi-axial deformation. Mechanical evaluation uses specimens with identical in-plane dimensions. Representative fabricated samples of both architectures appear in the optical images in **Figure 1E** and **Figure 1F**.

Device layouts (trace width of 10,20 & 30 μm) were generated as GDS files using a Python script based on the NIST nanolithography toolbox (Coimbatore Balram et al., 2016). Fabrication began on bare silicon wafers (University Wafer LLC) cleaned sequentially with acetone and isopropyl alcohol. Spin coating deposited a 2.5 μm-thick layer of polyimide (PI 2610, HD Microsystems), followed by curing at 380 °C to form the bottom encapsulation layer. Photolithography defined the metal interconnects using a bilayer resist stack consisting of SF5 and S1813 photoresists (Kayaku Advanced Materials). Broadband ultraviolet exposure (150 mJ cm^{-2}) and development in MF-26A produced the undercut profile required for lift-off. Electron beam evaporation (Kurt J. Lesker) deposited a Ti/Au (5 nm/100 nm) metal stack, and immersion in Remover PG completed the lift-off process. A second 2.5 μm-thick layer of PI 2610 encapsulated the metal traces, forming a PI/Au/PI structure with a total thickness of 5.1 μm. A hard-mask-assisted etching process defined the device geometry and contact openings. Spin coating deposited S1813 onto the PI surface, followed by baking at 110 °C for 10 min to remove residual solvent. Reactive sputtering deposited an 80 nm-thick aluminum hard mask. A second S1813 layer defined the device perimeter and contact openings by photolithography. Immersion in aluminum etchant (Sigma-Aldrich) transferred the pattern into the hard mask, and oxygen-plasma reactive ion etching removed the exposed polyimide, leaving the encapsulated interconnect network. The completed PI/Au/PI structures were transferred onto water-soluble tape (Aquasol Corporation) and treated with oxygen plasma. VM651 adhesion promoter was applied by atomized spray coating, followed by heating at 100 °C to remove residual solvent. Sequential spin coating of Ecoflex 00-30 (Smooth-On) and NuSil MED-6019 (Avantor), diluted with 10 vol% hexane, formed the final elastomeric substrate and backing layers. Immersion in deionized water dissolved the carrier tape and released the completed devices.

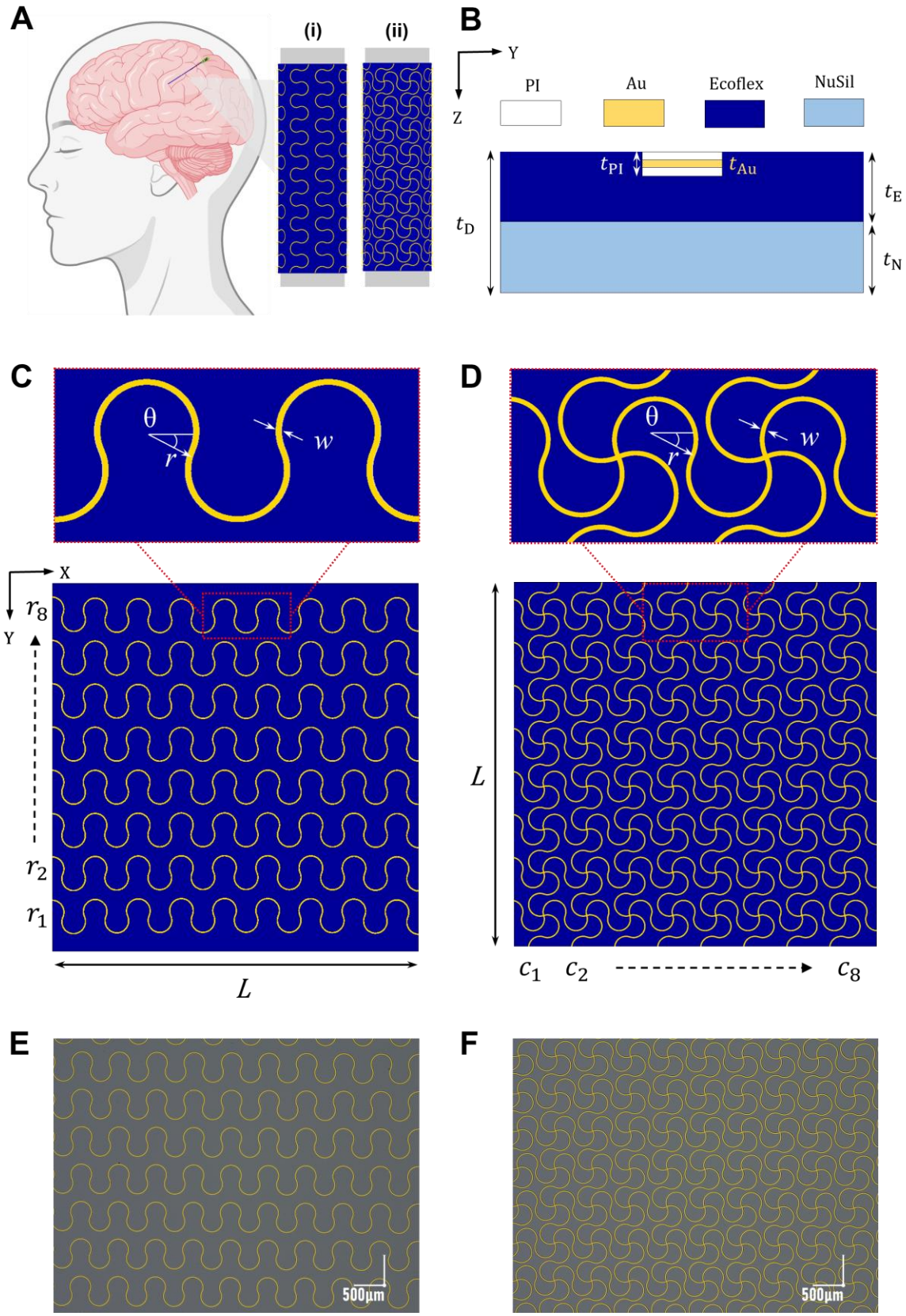

Figure 1. Design and fabrication of stretchable neural probe designs. (A) Schematic illustration of the intended neural probe application and the two investigated interconnect topologies: Single Serpentine Traces and Interconnected Mesh (Created in BioRender. https://BioRender.com/zp3he8z). **(B)** Cross-sectional architecture of the multilayer system comprising Au interconnects encapsulated within polyimide (PI), embedded in an Ecoflex substrate, and supported by a NuSil backing layer. **(C,D)** Geometric definitions of the serpentine unit cell, characterized by trace width w, arc radius r, and offset angle θ, for the Single Serpentine Traces and Interconnected Mesh architectures, respectively, along with the corresponding finite-element geometries used for mechanical analysis. **(E,F)** Optical micrographs of fabricated Single Serpentine Traces and Interconnected Mesh samples on silicon wafer. Scale bars: 500 μm.

Figure 2 demonstrates the conformability of the flexible electrode array wrapped around an 800 µm stainless steel guidewire illustrating its ability to accommodate the tight curvature without buckling or delamination. This structural integrity is critical for ensuring long-term interconnect reliability during implantation. Compared to conventional PMT SEEG electrodes, the proposed device architecture achieves a comparable form factor and maintains mechanical compliance with the surrounding tissue while offering the possibility of higher electrode sites densities.

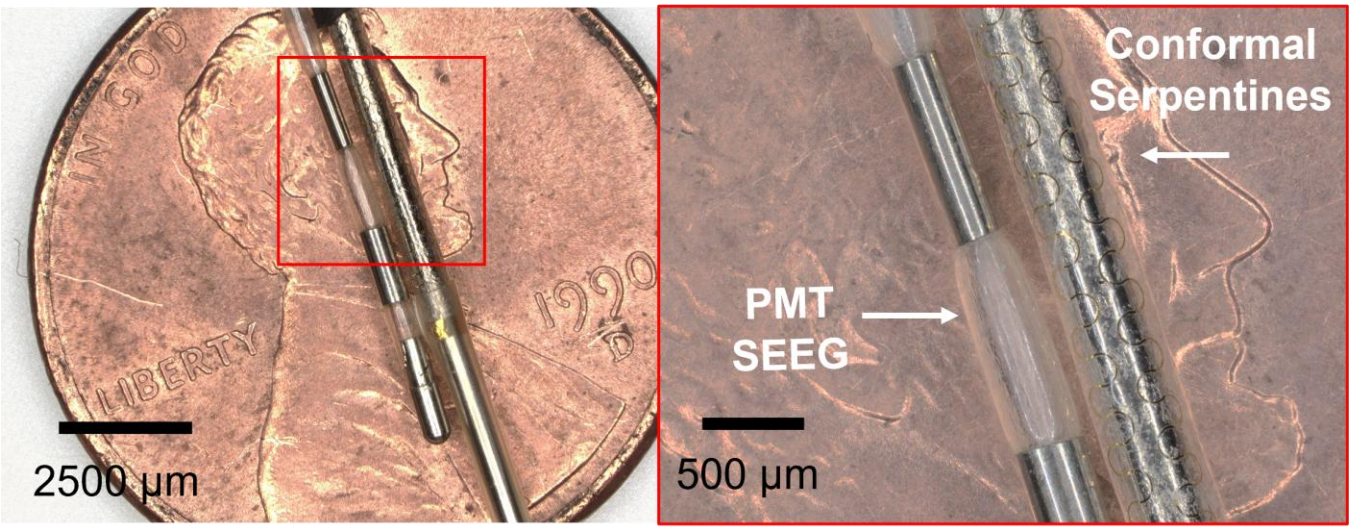

Figure 2. Wrapping mechanics and conformability of the neural probe architecture. (**Left**) Optical image of the interconnects in a cylindrical architecture wrapped around a 800 µm stainless steel guidewire demonstrating conformal integration onto a small-radius cylindrical substrate (scale bar: 2.5 mm) pictured next to PMT SEEG, the current clinical standard. Arrows indicate the Au serpentine interconnects distributed along the electrode shaft. **(Right)** Enlarged view of the mesh electrode highlighting the serpentine interconnect geometry that enables conformal wrapping (scale bar: 500 µm)

The Au interconnects are modeled as elastoplastic solids to capture yielding and fracture initiation under large deformation. The PI encapsulation layers are modeled as linear elastic materials because the strains remain well within the elastic regime. The Ecoflex substrate, NuSil backing layer, and PDMS cylindrical support are represented using incompressible hyperelastic constitutive laws based on the Mooney–Rivlin model

$$W = C_{10}(\bar{I}_1 - 3) + C_{01}(\bar{I}_2 - 3) + \frac{1}{D_1}(J - 1)^2 \quad (1)$$

where C_{10}, C_{01}, and D_1 are material parameters listed in Table 1. The elastoplastic response of the 100 nm Au film is obtained from an interpolated stress–strain relationship derived from tensile measurements of 55, 85, and 400 nm Au films reported by Kim et al. (2013). These experiments were performed on a water-supported platform that minimizes substrate constraint effects and therefore provides an intrinsic representation of thin-film mechanical behavior. The resulting stress–strain curve in **Figure 3** is used directly as the Au plastic constitutive input for the FEA simulations. The interpolated response yields a Young's modulus of $E_{Au} = 58.8$ GPa, a yield stress of $\sigma_{yield} = 202$ MPa, and a fracture stress of $\sigma_f \approx 429$ MPa. Throughout this study, σ_{yield} and σ_f serve as the primary criteria for evaluating the onset of plastic deformation and fracture within the serpentine interconnects.

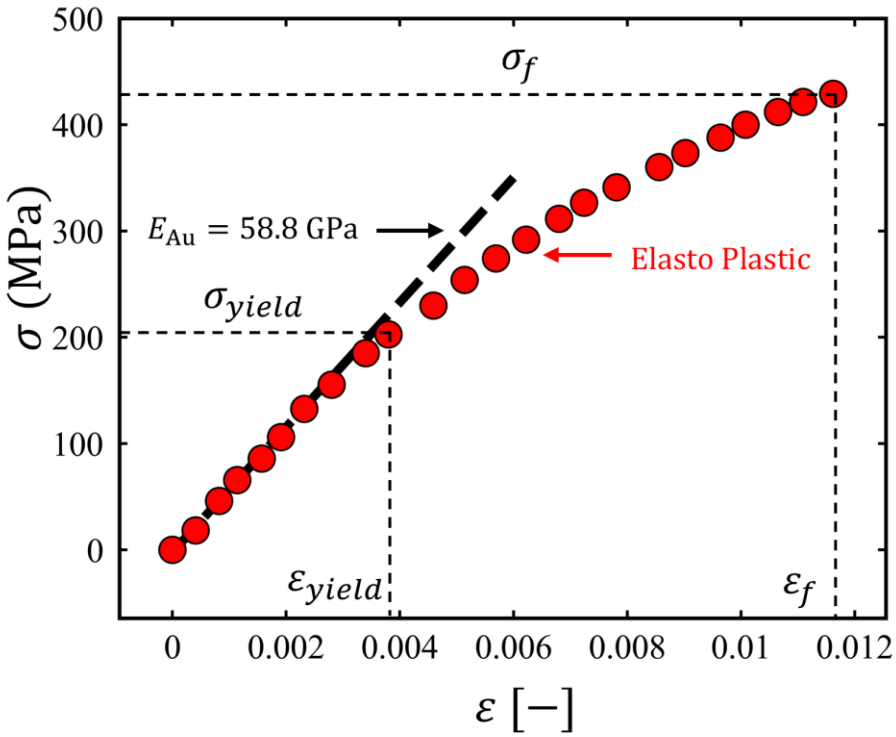

Figure 3. Stress–strain relation for the Au interconnects. The initial linear regime defines the elastic response, while subsequent strain hardening governs the post-yield behavior. The yield point $(\varepsilon_{yield}, \sigma_{yield})$ and fracture point $(\varepsilon_f, \sigma_f)$ provide the critical criteria for assessing the onset of plasticity and failure throughout the deformation analyses.

Table 1. Material properties and geometric parameters used in the finite element model

Material	Constitutive Model	Material Parameters			Thickness (μm)
Ecoflex 00-30	Mooney-Rivlin	C_{10} = 0.017 MPa	C_{01} = 0.004 MPa	D_1 = 0.960 MPa^{-1}	25
NuSil-Med-6019	Mooney-Rivlin	C_{10} = 1.21 MPa	C_{01} = 0.302 MPa	D_1 = 0.0133 MPa^{-1}	25
PDMS	Mooney-Rivlin	C_{10} = 0.243 68 MPa	C01 = 0.061 MPa	D_1 = 0.133 MPa^{-1}	-
Au	Elastoplastic	E = 58.8 GPa	v = 0.42	-	0.10
PI	Linear Elastic	E = 3.7 GPa	v = 0.34	-	5.0

2.2 Finite Element Analysis and Loading Conditions

The mechanical response of the Single Serpentine Traces and Interconnected Mesh designs is modeled using ABAQUS/Standard 2025. The multilayer geometry described in Section 2.1 is adopted in the finite element model. The Ecoflex and NuSil layers are discretized using eight-node linear brick elements with reduced integration (C3D8R). The PI/Au/PI interconnect stack is modeled as a layered composite shell using the ABAQUS Skin formulation, which captures the mechanical response of the ultrathin encapsulation and metallic trace layers while maintaining computational efficiency. Geometric nonlinearity (NLGEOM) is enabled in all simulations to capture the large deformations associated with stretching, cylindrical wrapping, and bending. A mesh convergence analysis confirms that the predicted stress distributions are independent of element size. Three loading conditions are considered: stretching, conformal wrapping, and post-wrapping bending. These loading modes represent deformation encountered during device handling, cylindrical integration, and chronic operation, respectively. The corresponding boundary conditions are described in the following sections, where all coordinates refer to the reference configuration.

2.2.1 Stretching Mechanics

The in-plane stretchability of the neural probe architectures is evaluated under displacement-controlled uniaxial and biaxial loading. For uniaxial stretching along the x-direction, equal and opposite displacements are prescribed on the boundaries $x = \pm L/2$ to generate a nominal engineering strain ε_x,

$$\mathbf{u}|_{x=\pm L/2} = \pm\frac{\varepsilon_x L}{2}\hat{\mathbf{e}}_{\boldsymbol{x}}, \qquad \varepsilon_x \in [0, 0.30]. \tag{2}$$

Similarly, uniaxial stretching along the y-direction is imposed through prescribed displacements on the boundaries $y = \pm L/2$,

$$\mathbf{u}|_{y=\pm L/2} = \pm\frac{\varepsilon_y L}{2}\hat{\mathbf{e}}_{y}, \qquad \varepsilon_y \in [0, 0.30]. \tag{3}$$

Equi-biaxial stretching is obtained by simultaneously applying both displacement fields. Rigid-body motion is suppressed through minimal displacement constraints applied to the substrate. The strain range of $0\% - 30\%$ encompasses deformation levels associated with device handling, cylindrical integration, and physiological tissue motion.

2.2.2 Wrapping Mechanics

The conformal integration process is simulated by wrapping the planar neural probe around cylindrical substrates with radii $R \in \{0.4, 0.5, 0.6, 0.7\}$ mm. The probe is initially positioned tangent to the cylindrical surface with its longitudinal axis aligned with the cylinder axis. To suppress rigid-body motion while allowing deformation during wrapping, the centerline of the bottom surface is constrained in the y- and z-directions,

$$u_y = u_z = 0, \qquad x = 0, -\frac{L}{2} \le y \le \frac{L}{2} \tag{4}$$

and the geometric center is additionally fixed in the x-direction $u_x(0,0,0) = 0$. The cylindrical substrate remains fixed throughout the simulation. **Figure 4** illustrates the sequential loading scheme used to generate conformal wrapping through equal and opposite rotations applied to reference points located at the two end surfaces,

$$\boldsymbol{\varphi}_R = -\varphi\hat{\mathbf{e}}_{\boldsymbol{x}}\,, \qquad \boldsymbol{\varphi}_L = +\varphi\hat{\mathbf{e}}_{\boldsymbol{x}}, \qquad \varphi \in [0, \pi] \tag{5}$$

where $\hat{\mathbf{e}}_{\boldsymbol{x}}$ denotes the cylinder axis and $\mathbf{X}_{\boldsymbol{c}} = (0, 0, R)$ defines the center of rotation. A small uniform pressure

$$p_0 \;=\; 2 \times 10^{-4}\,\mathrm{MPa} \tag{6}$$

facilitates contact initiation during the early stages of wrapping. Surface-to-surface contact between the probe and cylindrical substrate is modeled using finite-sliding kinematics with hard normal contact and rough tangential contact.

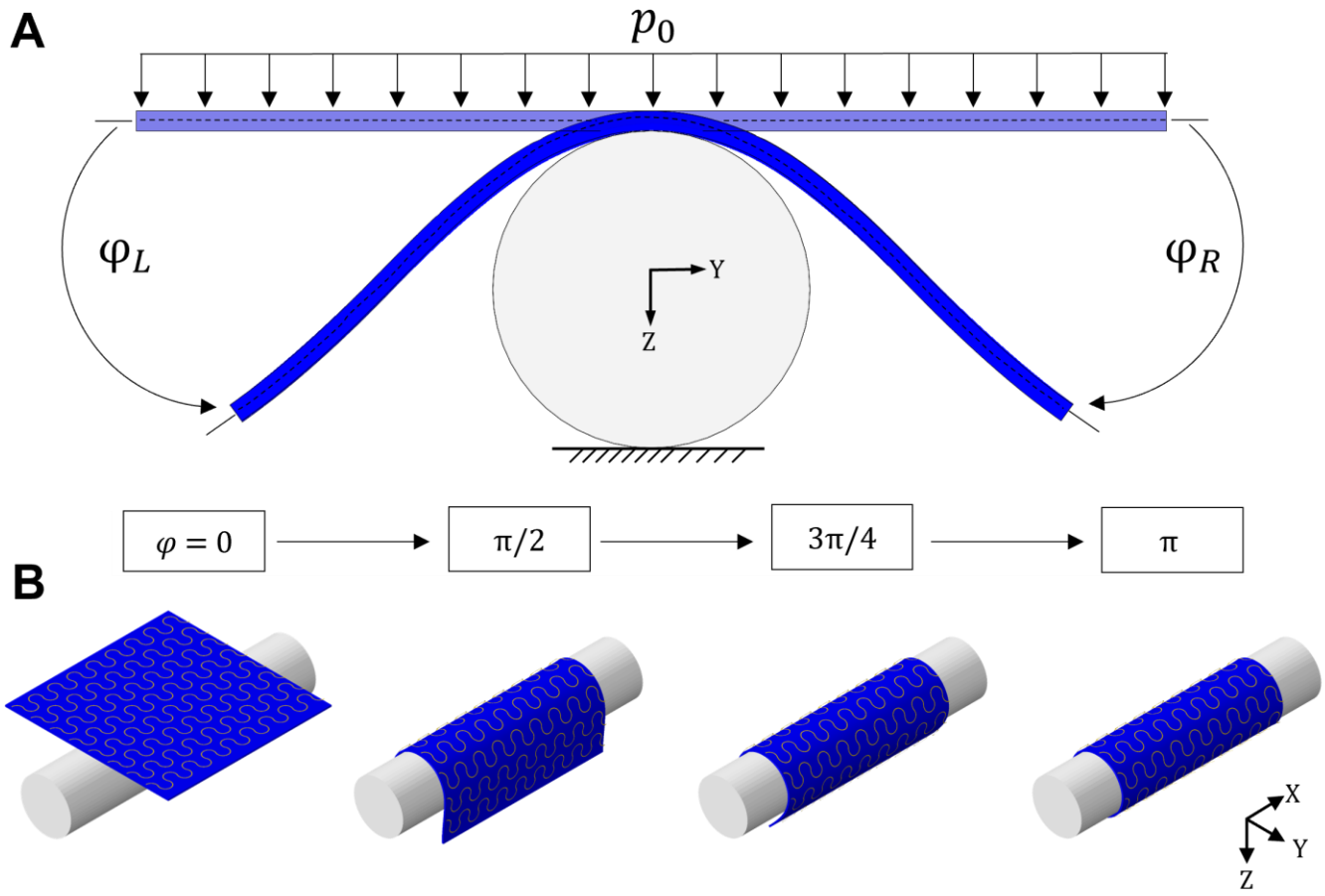

Figure 4. Geometry and loading sequence for conformal wrapping. (A) A planar serpentine mesh is transformed into a cylindrical configuration through prescribed end rotations about the probe axis. **(B)** Representative configurations at $\varphi = 0, \pi/2, 3\pi/4$, and π illustrate the progressive development of curvature and contact during integration onto the cylindrical substrate.

2.2.3 Bending Mechanics

The bending behavior of the conformally wrapped neural probe is modeled by subjecting the cylindrical substrate to cantilever deformation after completion of the wrapping process. The wrapped configuration serves as the initial state for all bending simulations. One end of the cylinder is fixed,

$$u_x = u_y = u_z = 0, \qquad \theta_x = \theta_y = \theta_z = 0 \tag{7}$$

while a transverse displacement is prescribed at the opposite end,

$$\mathbf{u} = \delta \hat{\mathbf{e}}_{\mathbf{z}}, \qquad \delta \in [0{,}15 \text{ mm}] \tag{8}$$

thereby generating curvature along the cylinder axis. The cylinder length is $l = 50$ mm and the position of the neural probe is characterized by the dimensionless coordinate $\frac{a}{l}$, where a denotes the distance between the fixed end and the center of the probe. Three representative locations are considered $a \in \left\{\frac{L}{2}, \frac{l}{2}, l - \frac{L}{2}\right\}$. This parameterization isolates the influence of local bending curvature on stress development within the conformal serpentine architecture and enables systematic evaluation of how probe location affects stress localization within the interconnect network.

3 RESULTS AND DISCUSSION

3.1 Mechanics of Uniaxial Stretching

Figure 5 presents the mechanical response of the Single Serpentine Traces and Interconnected Mesh architectures under uniaxial stretching in the x-direction. The figure includes full-field von Mises stress distributions at $\varepsilon_x = 10\%$ (**Figs. 5A** and **5B**), corresponding experimental images of the deformed structures (**Figs. 5C** and **5D**), and stress profiles along the inner curved path L_{AB} and transverse cross-sectional path W_{CD} at four strain levels (**Figs. 5E–H**). The selected strain levels ($\varepsilon_x = 5\%, 10\%, 25\%, 30\%$) capture the transition from elastic deformation to yielding and eventual fracture initiation.

At $\varepsilon_x = 10\%$, the stress distributions in **Fig. 5A** and **5B** reveal that deformation is dominated by bending of the horseshoe arcs. Consequently, the maximum stress localizes at the crown of the arc, where curvature changes most rapidly during stretching. The inner curvature consistently experiences slightly higher stress than the outer curvature, whereas the lower connecting segments remain comparatively unstressed. The experimentally observed deformation modes in **Fig. A1** and **Fig. 5C-5D** agree closely with the finite element predictions, confirming that the simulations accurately capture the dominant bending and rotation mechanisms governing serpentine deformation. This behavior motivates the selection of the inner arc path L_{AB} as the primary evaluation path. In the Single Serpentine Traces architecture, stress decreases rapidly away from the crown toward points A and B (**Fig. 5E**), indicating efficient redistribution of deformation through rotational motion of the serpentine geometry. The Interconnected Mesh architecture exhibits a similar primary stress concentration at the crown of the arc; however, the orthogonal interconnections introduce an additional stress concentration near point B (**Fig. 5F**). This secondary peak arises from geometric constraint imposed by the intersecting serpentine columns, which restrict local rotational freedom and increase stress transfer through the junction region. Despite this additional concentration, the crown of the arc remains the dominant critical location in both architectures.

The transverse path W_{CD}, positioned at the crown of the arc, provides additional insight into the local stress state. As shown in **Fig. 5G** and **5H**, the highest stresses occur near the inner and outer surfaces of the trace, whereas the central region experiences substantially lower stress levels. This distribution is characteristic of curvature-induced bending, where the largest tensile and compressive strains develop furthest from the neutral axis. The evolution of stress with increasing strain reveals the progression from elastic deformation to yielding and fracture initiation. At $\varepsilon_x = 5\%$, stresses remain below the yield strength of Au ($\sigma_{yield} = 202$ MPa) throughout both architectures, indicating fully elastic behavior (**Fig. 5E–H**). Increasing the strain to $\varepsilon_x = 10\%$ causes the crown stress to exceed σ_{yield}, marking the onset of plastic deformation in both designs (**Fig. 5E** and **5F**). In the Interconnected Mesh architecture, the secondary stress concentration at the junction also exceeds the yield threshold, indicating simultaneous yielding at the crown and interconnection region. The corresponding cross-sectional stress profiles indicate that yielding initiates at the inner and outer surfaces while the core of the trace remains elastic, consistent with curvature-dominated bending of the serpentine geometry (**Fig. 5G** and **5H**).

At $\varepsilon_x = 25\%$, stresses exceed σ_{yield} over most of the path L_{AB} and across the entire cross section W_{CD}, indicating extensive plastic deformation throughout the serpentine structure (**Fig. 4E–H**). Nevertheless, stresses remain below the fracture strength of Au ($\sigma_f \approx 429$ MPa), suggesting that structural integrity is maintained despite significant yielding. At $\varepsilon_x = 30\%$, the stress at the crown of the arc reaches σ_f in both architectures, indicating fracture initiation at this location (**Fig. 5E** and **5F**). Although the junction stress in the Interconnected Mesh architecture increases substantially, it remains below the fracture threshold. These results identify the crown of the serpentine arc as the governing failure location under uniaxial stretching regardless of interconnect topology. Overall, yielding initiates between $\varepsilon_x = 5\%$ and 10% in both architectures, establishing $\varepsilon_0 = 10\%$ as the critical strain level separating predominantly elastic and plastic deformation. This strain level is therefore adopted as the reference condition in **Fig. 6**, where the analysis is extended to uniaxial loading in the y-direction and equal biaxial stretching to evaluate the influence of loading mode on stress localization and failure behavior.

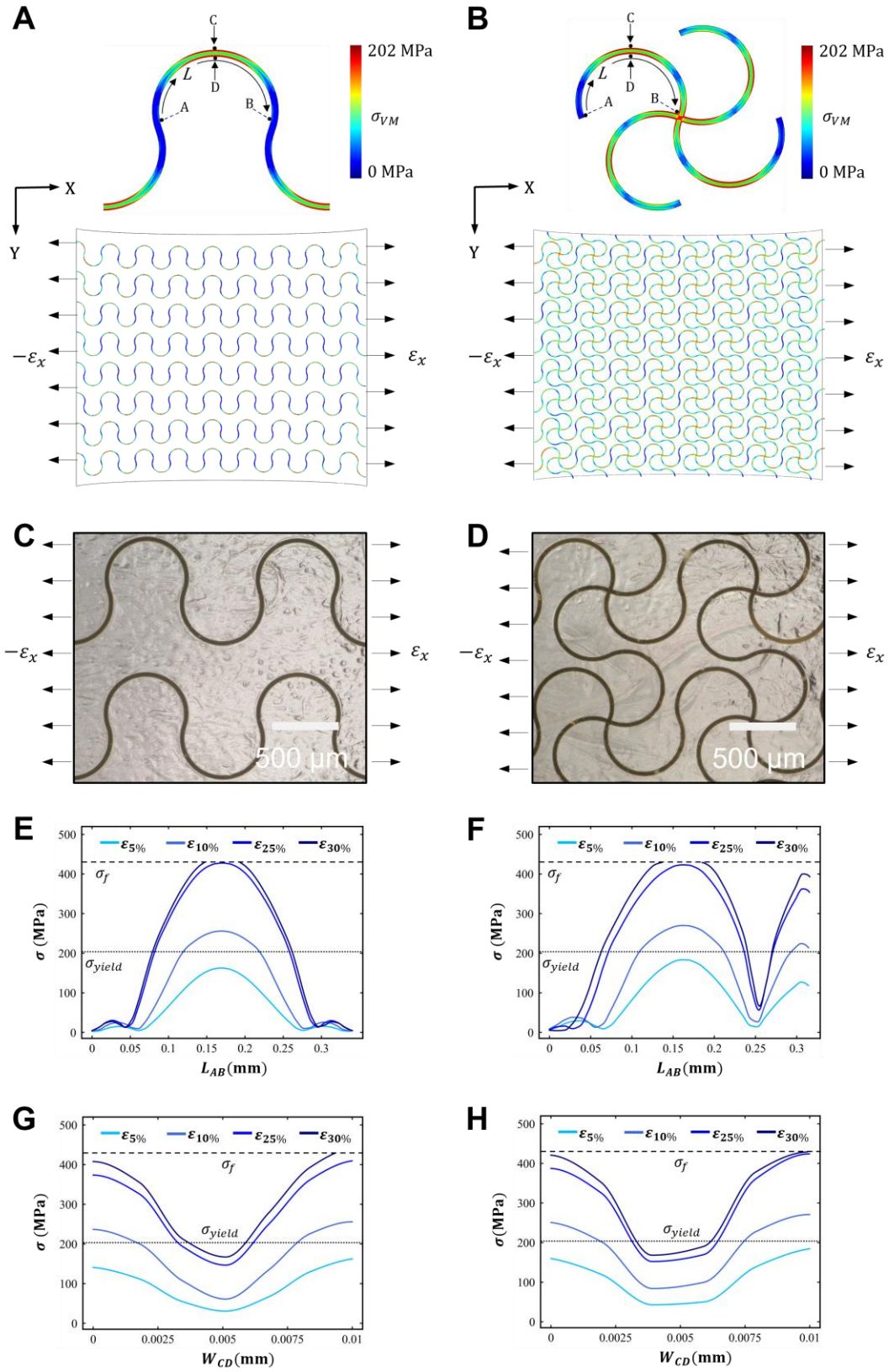

Figure 5. Uniaxial stretching mechanics of the Single Serpentine Traces and Interconnected Mesh architectures. **(A,B)** Deformed configurations and von Mises stress distributions in the Au interconnects at $\varepsilon_x = 30\%$, with enlarged views of representative serpentine unit cells. The paths L_{AB} and W_{CD} define the directions used for stress analysis. **(C,D)** Experimental images of the corresponding stretched configurations at $\varepsilon_x = 30\%$. **(E,F)** Stress profiles along L_{AB} and **(G,H)** stress profiles along W_{CD} for applied strains ranging from 5% to 30%. Dashed and dotted horizontal lines indicate the fracture and yield stresses of Au, respectively.

3.2 Loading Direction Effects on Stress Localization

Figure 6 compares the stress distributions in the Au interconnects and Ecoflex substrate under uniaxial loading in the x- and y-directions and equi-biaxial stretching at the critical strain level $\varepsilon_0 = 10\%$. Whereas **Fig. 5** established the onset of yielding within the Au traces, **Fig. 6** details how loading direction and interconnect topology govern stress transfer from the conductive network into the surrounding substrate. The Au traces are evaluated using von Mises stress, whereas the substrate response is characterized by the maximum principal stress because the Ecoflex experiences both tensile and compressive deformation. The principal stress metrics extracted from the Au interconnects and Ecoflex substrate at $\varepsilon_0 = 10\%$ are summarized in **Table 2**. **Table 2** highlights a key distinction between the two architectures: while the mean stress differs only modestly across loading conditions, the peak stress varies substantially, indicating that local geometric constraints rather than global deformation govern failure initiation.

Table 2. Summary of stress metrics at $\varepsilon_0 = 10\%$ for both stretchable serpentine architectures.

Architecture	Loading Condition	Au mean σ_{vm} (MPa)	Au peak σ_{vm} (MPa)	Ecoflex mean σ (MPa)	Ecoflex peak σ (MPa)
Single Serpentine Traces	x-direction	68.8	256.5	0.013	0.068
Single Serpentine Traces	y-direction	74.2	223.0	0.015	0.148
Single Serpentine Traces	Biaxial	93.8	224.6	0.027	0.229
Interconnected Mesh	x-direction	95.6	271.1	0.018	0.181
Interconnected Mesh	y-direction	95.6	271.1	0.018	0.181
Interconnected Mesh	Biaxial	88.4	220.6	0.036	0.259

For the Single Serpentine Traces architecture, the deformation mechanism depends strongly on loading direction. Under x-direction stretching (**Fig. 6A**), deformation is accommodated primarily through bending and rotation of the horseshoe arcs, resulting in localized yielding at the arc crown while maintaining relatively low substrate stresses. Loading in the y-direction (**Fig. 6C**) suppresses this bending mode and forces a larger fraction of the deformation into the surrounding Ecoflex. Consequently, the peak substrate stress increases by approximately 2.2-fold relative to the x-direction case (0.148 MPa versus 0.068 MPa) despite only modest changes in the peak stress within the Au traces (Table 2). Under biaxial loading (**Fig. 6E**), simultaneous stretching in both directions partially cancels tensile and compressive stresses along portions of the arc, reducing stress along the outer curvature while concentrating stress along the inner curvature. Although the peak trace stress remains comparable to the uniaxial cases, the substrate experiences its highest stress levels, with peak stresses approximately 3.4 times greater than those under x-direction loading (0.229 MPa versus 0.068 MPa) because the serpentine geometry can no longer efficiently accommodate deformation through bending in either direction.

The Interconnected Mesh architecture exhibits a fundamentally different response because of its geometric symmetry and orthogonal interconnections. Under uniaxial loading (**Fig. 6B** and **6D**), the stress fields for the x- and y-directions are nearly identical apart from a $90°$rotation, consistent with the symmetric 8×8 topology. Additional stress concentrations develop at the interconnection junctions, where rotational compliance is restricted and deformation is transferred between intersecting serpentine segments. As a result, peak substrate stresses increase from 0.068 MPa in the Single Serpentine Traces architecture to 0.181 MPa in the Interconnected Mesh architecture, corresponding to an approximately 2.7-fold increase in stress transfer to the substrate (**Table 2**). Under biaxial loading (**Fig. 6F**), stress remains concentrated along the inner arc curvatures and junction regions. Similar to the Single Serpentine Traces architecture, partial stress cancellation reduces the peak trace stress, but the substrate experiences the most severe stress concentrations among all loading conditions, reaching a maximum principal stress of 0.259 MPa, approximately 1.13 times higher than the corresponding biaxial response of the Single Serpentine Traces architecture (0.229 MPa). This increase reflects the limited strain-accommodation capacity of the interconnected network under simultaneous loading in both directions.

The maximum-stress curves in **Fig. 6G** and **6H** quantify the influence of loading direction on stretchability. For the Single Serpentine Traces architecture, loading along the x-direction produces the highest trace stresses and therefore governs yielding, with localized yielding initiating at approximately $\varepsilon_{yield} \approx 6.25\%$. Yielding under y-direction and biaxial loading is delayed to approximately $\varepsilon_{yield} \approx 8.25\%$. In contrast, the Interconnected Mesh architecture exhibits nearly identical responses under x- and y-direction loading owing to geometric symmetry, with yielding initiating at approximately $\varepsilon_{yield} \approx 5.5\%$. The biaxial response lies below the uniaxial curves and delays yielding to approximately $\varepsilon_{yield} \approx 8.25\%$.

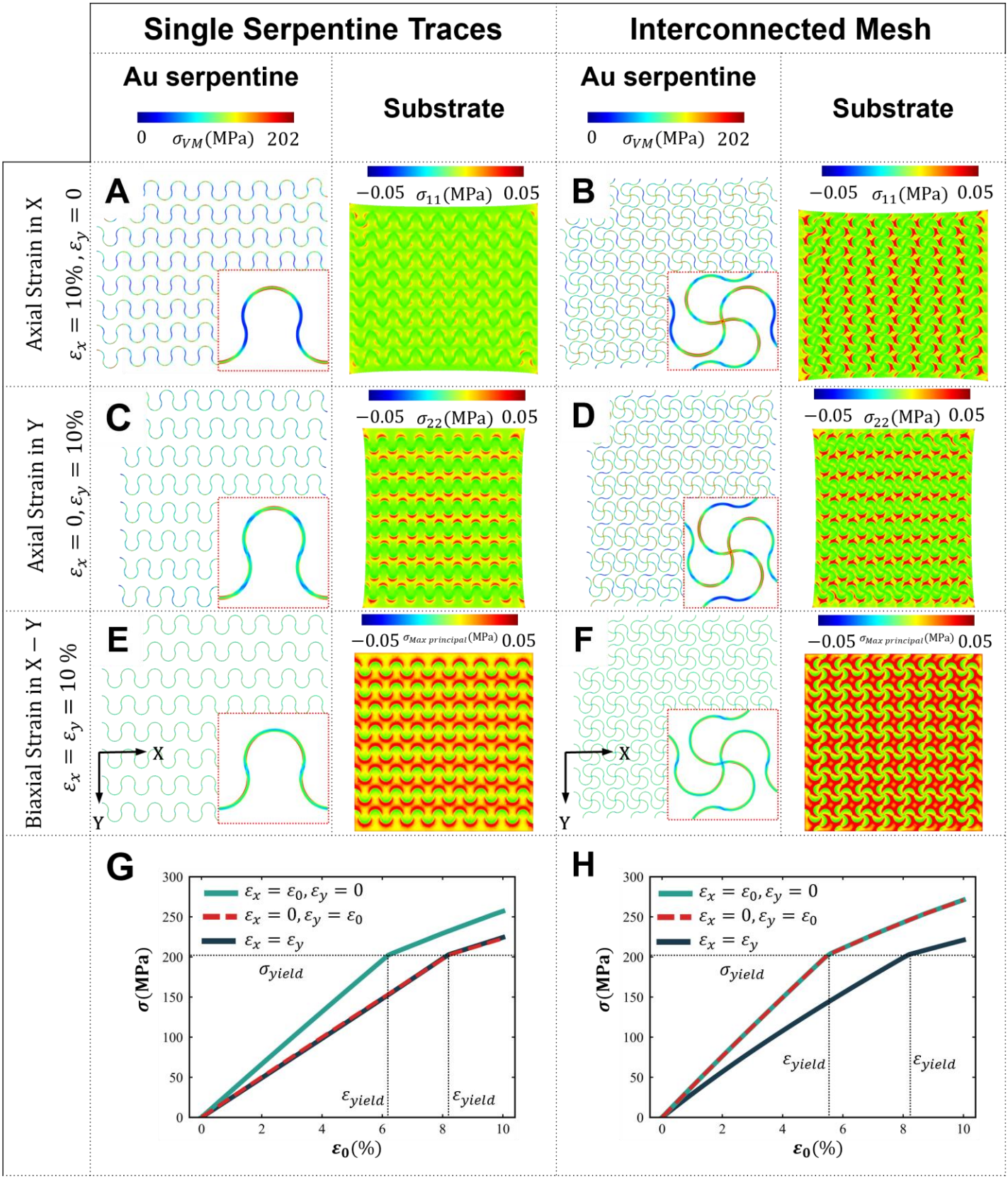

Figure 6. Loading-direction dependence of stress localization in stretchable neural probe architectures. (A–F) Stress distributions in the Au interconnects and substrate for uniaxial x-direction stretching, uniaxial y-direction stretching, and equal biaxial stretching at $\varepsilon_0 = 10\%$. Insets highlight representative serpentine unit cells and the associated stress concentrations. **(G,H)** Maximum interconnect stress as a function of applied strain for the three loading modes. The dashed horizontal line denotes the Au yield stress, defining the onset of plastic deformation.

Although the substrate stresses are substantially lower than those developed within the Au interconnects, their magnitude remains relevant when considering potential mechanical interactions with surrounding neural tissue. Typical somatosensory and mechanotransduction responses are often associated with local stress levels on the order of tens of kilopascals. The peak substrate stresses predicted in this study range from approximately 68–259 kPa (**Table 2**), locally exceeding commonly reported mechanosensory stress ~20 kPa (Chung et al., 2020, 2019). Although tissue deformation is not modeled explicitly, these results suggest that interconnect topology may influence not only device reliability but also the local mechanical environment experienced by surrounding neural tissue (Sridharan et al., 2013b). Collectively, these results demonstrate that interconnect topology governs not only stress localization within the Au traces but also the transfer of deformation into the surrounding substrate. The Single Serpentine Traces architecture provides greater rotational compliance and reduced substrate loading, whereas the Interconnected Mesh architecture promotes more uniform in-plane strain accommodation at the expense of elevated substrate stress concentrations. Across both architectures, biaxial loading produces the most severe substrate stress despite not generating the highest trace stresses, highlighting a fundamental tradeoff between interconnect protection and substrate mechanics.

3.3 Conformal Wrapping onto Cylindrical Neural Probes

Wrapping around cylindrical probes represents a critical deployment step for implantable neural interfaces and introduces a deformation mode fundamentally different from in-plane stretching. Whereas stretching primarily loads the serpentine traces through in-plane bending and rotation, cylindrical wrapping imposes curvature across the thickness of the multilayer structure, simultaneously placing the outer surface in tension and the inner surface in compression. To evaluate the influence of curvature, both architectures are wrapped around cylindrical substrates with radii R =0.4, 0.5, 0.6, and 0.7 mm that correspond to clinically relevant neural probe dimensions. The smallest case ($R = 0.4$ mm) is shown in **Fig. 7A** and **7B** together with the corresponding experimental images (**Fig. 7C** and **7D**). **Figure 7E** summarizes the mean, maximum, and minimum von Mises stresses as a function of cylinder radius.

For the Single Serpentine Traces architecture, wrapping-induced stress is distributed relatively uniformly along the horseshoe arcs, with moderate localization at the crown and side curvatures (**Fig. 7A**). Despite the severe curvature associated with $R = 0.4$ mm, the maximum stress remains below the Au yield strength ($\sigma_{yield} = 202$ MPa), indicating that the architecture can conformally wrap around all investigated probe radii without plastic deformation. In contrast, the Interconnected Mesh architecture develops additional stress concentrations at the interconnection junctions (**Fig. 7B**). These regions restrict local rotational compliance and transfer deformation between orthogonal serpentine segments, producing localized stress amplification. Consequently, the maximum stress reaches approximately 215 MPa at $R = 0.4$ mm, locally exceeding σ_{yield}, whereas the corresponding maximum stress in the Single Serpentine Traces architecture remains limited to approximately 145 MPa. This nearly 50% increase in peak stress demonstrates that topology, rather than average curvature alone, governs the onset of yielding during conformal wrapping. Importantly, the mean stress differs only modestly between the two architectures, whereas the peak stress differs by nearly 50%, indicating that local geometric constraints dominate failure initiation during deployment.

Figure 7E further reveals that the mean stress decreases approximately linearly with increasing cylinder radius for both architectures, reflecting the inverse relationship between bending strain and curvature. The nearly identical mean-stress sensitivities of the two designs indicate that the global bending response is primarily controlled by the overall stiffness of the multilayer stack. In contrast, the maximum stresses differ substantially because local topology governs stress localization. As a result, the mean stress alone provides a poor predictor of mechanical reliability, whereas the peak stress directly captures the influence of geometric constraints introduced by the interconnection network. The asymmetry between the tensile and compressive stress bounds provides additional insight into the mechanics of the wrapped structures. For both architectures, tensile stresses increase substantially more rapidly with curvature than compressive stresses. This behavior reflect the Au traces position above the neutral axis of the multilayer stack residing predominantly on the tensile side during wrapping. As curvature increases, the traces experience a disproportionately larger increase in tensile strain than the corresponding compressive strain developed at the inner surface. The effect is particularly pronounced in the Interconnected Mesh architecture, where junction-induced constraints further amplify local tensile stresses.

From a design perspective, these results demonstrate that conformal wrapping is considerably less demanding than in-plane stretching for both architectures. Even at the smallest radius investigated ($R = 0.4$ mm), corresponding to a probe diameter of only 0.8 mm and a curvature of 2.5 mm^{-1}, yielding is completely avoided in the Single Serpentine Traces architecture and remains confined to small, localized junction regions in the Interconnected Mesh architecture. More importantly, the results reveal a fundamental tradeoff between electrical connectivity and mechanical robustness: increasing interconnect density through orthogonal coupling enhances network connectivity but introduces geometric constraints that significantly elevate peak stresses during deployment. These findings identify the Single Serpentine Traces architecture as the more mechanically robust design for conformal integration onto small-diameter neural probes and demonstrate that rotational compliance, rather than average curvature accommodation, governs resistance to yielding during fabrication and operation.

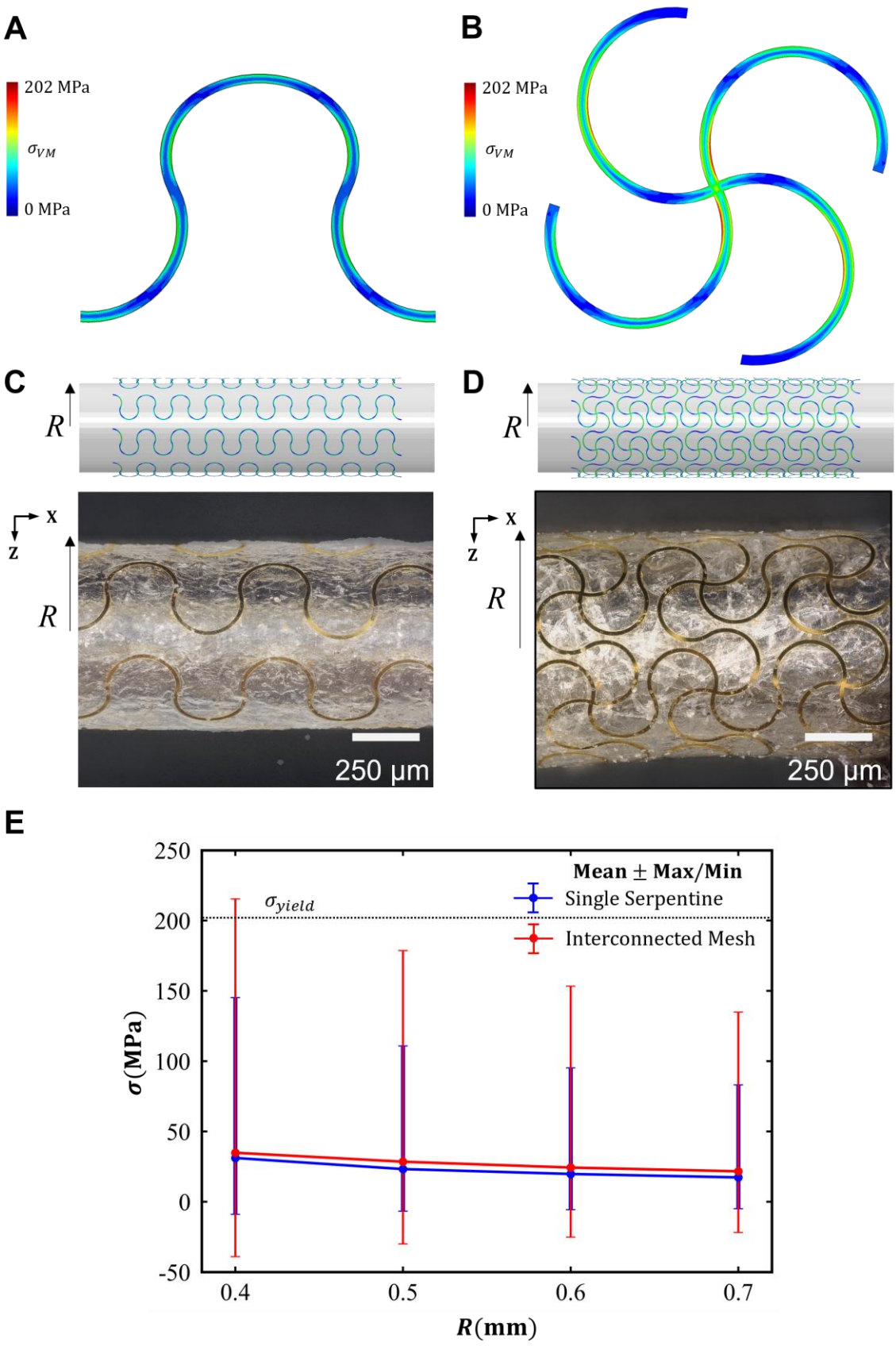

Figure 7. Mechanics of conformal wrapping onto cylindrical neural probes. (A,B) Interconnect stress distributions for the Single Serpentine Traces and Interconnected Mesh architectures wrapped around a probe of radius $R = 0.4$ mm. **(C,D)** Experimental images of the corresponding wrapped configurations. **(E)** Mean, maximum, and minimum interconnect stresses as a function of cylinder radius ($R = 0.4 - 0.7$ mm) for both architectures. Bars denote the max/min range of the stress distribution within the Au interconnects. The horizontal dashed line indicates the Au yield stress.

3.4 Bending Mechanics of Conformally Wrapped Neural Probes

Following conformal integration onto the cylindrical substrate, the mechanical response of the wrapped neural probes is evaluated under cantilever bending. Three normalized probe locations along the cylinder axis are considered, $\frac{a}{l} = 0.0, 0.5$ and 1.0 (**Fig. 8A**). Because the most demanding wrapping condition occurred at $R = 0.4$ mm (**Fig. 7**), all bending simulations are performed using this radius. Sequential deformation configurations corresponding to 0.25δ, 0.5δ, 0.75δ, and δ are shown in **Fig. 8B**. The resulting von Mises stress distributions at the most critical location ($a/l = 0.5$) are presented in **Fig. 8C** and **8D** for the Single Serpentine Traces and Interconnected Mesh architectures, respectively, while **Fig. 8E** and **8F** summarize the evolution of stress with applied tip displacement.

For both architectures, the stress increases approximately linearly with applied displacement, indicating that the wrapped structures operate within a bending-dominated regime over the investigated displacement range. However, the magnitude of the response depends strongly on probe location. The lowest stress sensitivity occurs near the fixed end ($\frac{a}{l} = 0.0$), where the local deformation of the wrapped region is constrained by the clamped boundary condition. As the probe is moved toward the mid-span of the cantilever, it experiences a larger bending moment and therefore greater local curvature, producing the highest stress sensitivity at $\frac{a}{l} = 0.5$. Beyond this location, the sensitivity decreases again as the probe approaches the free end ($\frac{a}{l} = 1.0$). These results identify the mid-span region as the most mechanically demanding location for chronic bending of conformally integrated neural interfaces.

The influence of topology is evident when comparing the two architectures. For the Single Serpentine Traces architecture (**Fig. 8E**), stress sensitivity increases from $m \approx 0.022$ MPa/mm at $\frac{a}{l} = 0.0$ to $m \approx 0.089$ MPa/mm at $\frac{a}{l} = 0.5$, corresponding to an approximately fourfold increase in curvature sensitivity. The sensitivity then decreases to $m \approx 0.040$ MPa/mm at $\frac{a}{l} = 1.0$. In contrast, the Interconnected Mesh architecture exhibits consistently higher sensitivities across all probe locations (**Fig. 8F**), increasing from $m \approx 0.040$ MPa/mm at $\frac{a}{l} = 0.0$ to $m \approx 0.198$ MPa/mm at $\frac{a}{l} = 0.5$, before decreasing to $m \approx 0.089$ MPa/mm at $\frac{a}{l} = 1.0$. The approximately twofold increase in sensitivity relative to the Single Serpentine Traces architecture demonstrates that the orthogonal interconnections significantly amplify curvature-induced stress development during bending.

The stress distributions in **Fig. 8C** and **8D** provide insight into the underlying mechanism. Similar to the wrapping response shown in **Fig. 7**, stress localizes primarily within the curved serpentine segments. However, the Interconnected Mesh architecture develops additional concentrations at the interconnection junctions, where deformation compatibility between intersecting traces restricts local rotation and promotes stress transfer across the network. Consequently, the same geometric features that increased stress during cylindrical wrapping continue to govern stress amplification during subsequent bending.

From a design perspective, these results demonstrate that the mechanical penalty associated with increased interconnect density extends beyond the deployment phase. Although the Interconnected Mesh architecture provides enhanced connectivity, it remains consistently more sensitive to curvature-induced deformation during both wrapping and post-deployment bending. In contrast, the Single Serpentine Traces architecture maintains lower stress sensitivities across all probe locations owing to its greater rotational compliance. These findings demonstrate that probe placement and interconnect topology jointly govern curvature-induced stress amplification and should therefore be considered simultaneously when designing mechanically compliant neural interfaces.

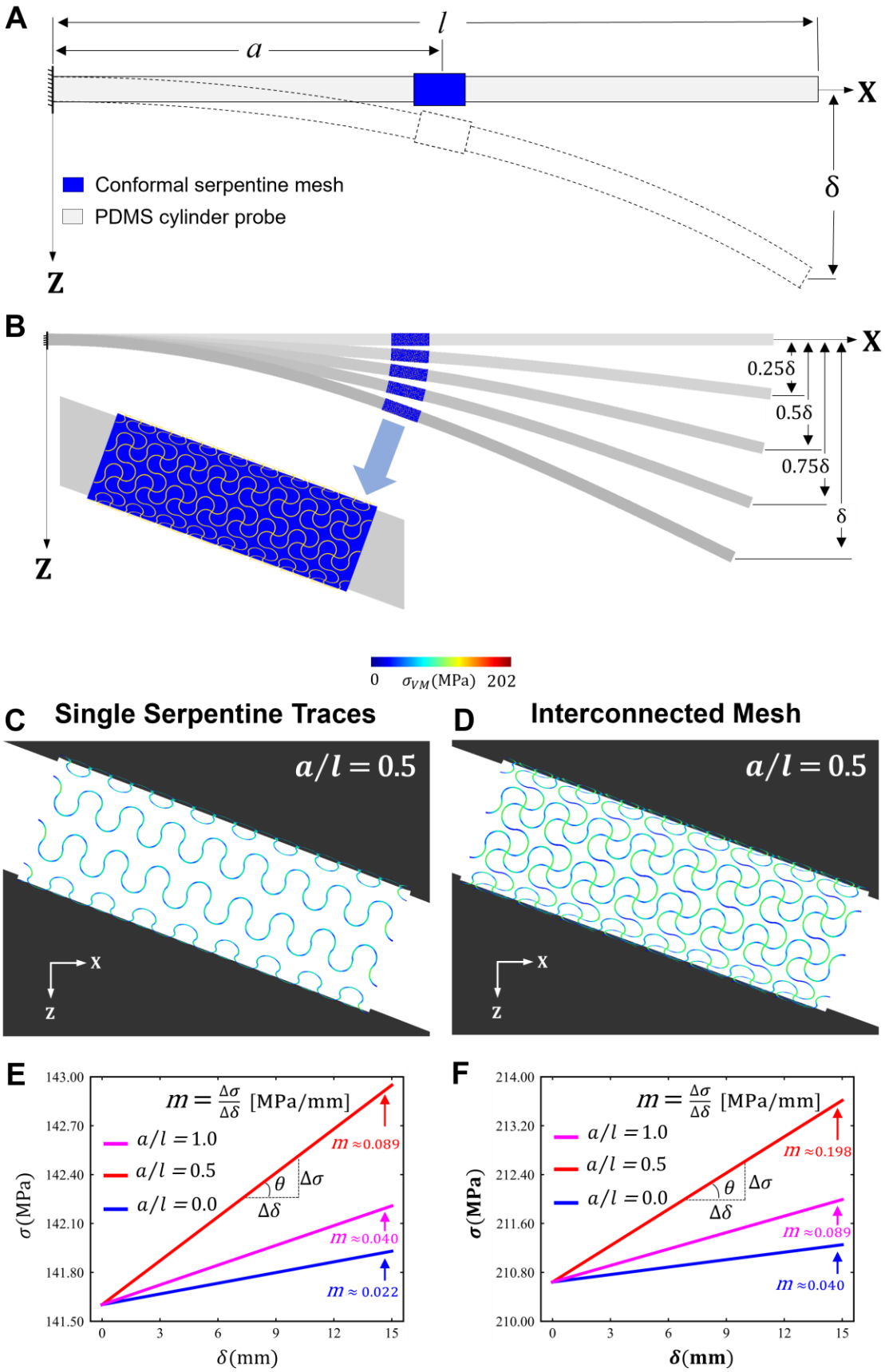

Figure 8. Bending mechanics of conformally wrapped neural probes. (A) Cantilever bending configuration and definition of the normalized probe position a/l. **(B)** Representative deformation sequence under increasing tip displacement. **(C,D)** Stress distribution in the Au interconnects for the deformed configurations of the Single Serpentine Traces and Interconnected Mesh architectures at $a/l = 0.5$. **(E,F)** Maximum interconnect stress as a function of tip displacement for different probe locations. The slope $m = \Delta\sigma/\Delta\delta$ characterizes the sensitivity of the interconnect stress to bending-induced curvature.

3.5 Combined Effects of Wrapping and Bending

Figure 9 compares the maximum von Mises stress in the wrapped state and after subsequent bending at the three normalized probe locations. For the Single Serpentine Traces architecture (**Fig. 9A**), bending produces only a negligible increase in stress relative to the wrapped configuration. The maximum stress increases from 141.6 MPa in the wrapped state to a peak value of 142.9 MPa at $\frac{a}{l} = 0.5$, corresponding to an increase of less than 1%. Consequently, the stress remains well below the Au yield strength under all combined loading conditions. The Interconnected Mesh architecture (**Fig. 9B**) exhibits a similar positional trend but at substantially higher stress levels. The wrapped configuration already reaches 210.6 MPa, slightly exceeding σ_{yield} because of localized stress concentrations at the interconnection junctions. Subsequent bending produces only a modest increase in stress, with the maximum value reaching 213.6 MPa at $\frac{a}{l} = 0.5$. Although bending amplifies the existing stress concentrations, the increase remains small relative to the stress generated during the wrapping process. Overall, the results demonstrate that curvature, rather than subsequent physiological bending, constitutes the dominant mechanical loading condition for both architectures. Consequently, optimization of the wrapping process and mitigation of junction-induced stress concentrations are likely to provide greater improvements in long-term reliability than further reductions in bending sensitivity.

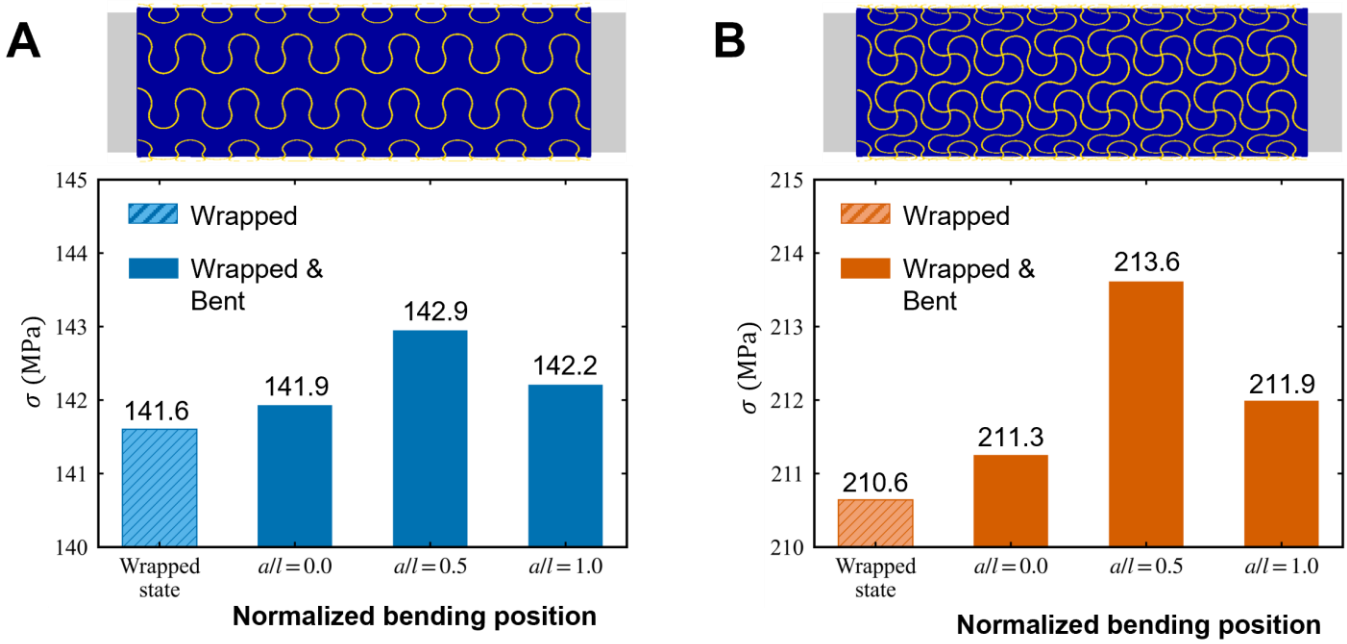

Figure 9. Relative contributions of wrapping and bending to stress development in conformal neural probes. (A) Single Serpentine Traces. **(B)** Interconnected Mesh. Maximum interconnect stresses are shown for the wrapped state and after bending at different normalized probe locations. The comparison isolates the incremental stress associated with bending-induced curvature from that generated during conformal wrapping.

Collectively, **Figs. 5–9** reveal a consistent trend across stretching, wrapping, and bending: geometric constraints introduced by interconnection junctions systematically amplify stress localization. Although the Interconnected Mesh architecture provides enhanced electrical connectivity, the Single Serpentine Traces architecture maintains lower peak stresses under all loading modes owing to its greater rotational compliance. This tradeoff between electrical connectivity and mechanics emerges as a central design consideration for conformal neural interfaces and highlights the importance of topology and mechanical design in stretchable bioelectronics.

4. CONCLUSION

Finite element analysis and experimental optical images were used to examine the mechanics of two representative stretchable neural interface architectures subjected to stretching, conformal wrapping, and bending. Stress concentrations were controlled primarily by serpentine-interconnect topology. The Single Serpentine Traces architecture accommodated deformation through rotation and bending of the serpentine segments, resulting in lower peak stresses and delayed yielding. The Interconnected Mesh architecture exhibited larger stress concentrations at interconnection junctions where local rotational freedom was constrained. Wrapping onto small-radius (0.4 mm) cylindrical probes was identified as the most mechanically demanding loading condition, whereas subsequent bending from probe manipulation contributed only a small increase in stress. The results demonstrate that rotational compliance governs mechanical reliability and establish the tradeoff between network connectivity and stress localization that must be balanced in the design of future conformal sub-millimeter-scale neural interfaces.

Acknowledgment

This research is funded in part through an award from the Rice Office of Research & the Rice Brain Institute DPRIT Seed Grant Program. S.B. acknowledges financial support from the Bolashak International Scholarship Program (JSC Center for International Programs, Kazakhstan). P.V.P. and J.P.S. acknowledge funding support from the NIH NINDS under awards RF1NS133972 and UG3NS12548. This work was done in part using resources of the Shared Equipment Authority at Rice University (https://research.rice.edu/sea/). We thank the Rice Cleanroom Staff for the use of their facilities.

CRediT authorship contribution statement

Sagidolla Batay: Conceptualization, Methodology, Software, Validation, Formal Analysis, Investigation, Writing – Original Draft, Visualization. **Yulin Zhou**: Conceptualization, Methodology, Software, Investigation. **Priyan V. Pathirana**: Conceptualization, Methodology, Validation, Formal Analysis, Investigation. **John P. Seymour**: Conceptualization, Resources, Writing – Review & Editing, Supervision, Project Administration, Funding Acquisition. **Raudel Avila:** Conceptualization, Methodology, Resources, Writing – Original Draft, Writing – Review & Editing, Supervision, Project Administration, Funding Acquisition.

Declaration of competing interest

The authors declare that they have no known competing financial interests or personal relationships that could have appeared to influence the work reported in this paper.

Data Availability

All data generated or analyzed during this study are included in this published article.

Appendix 1

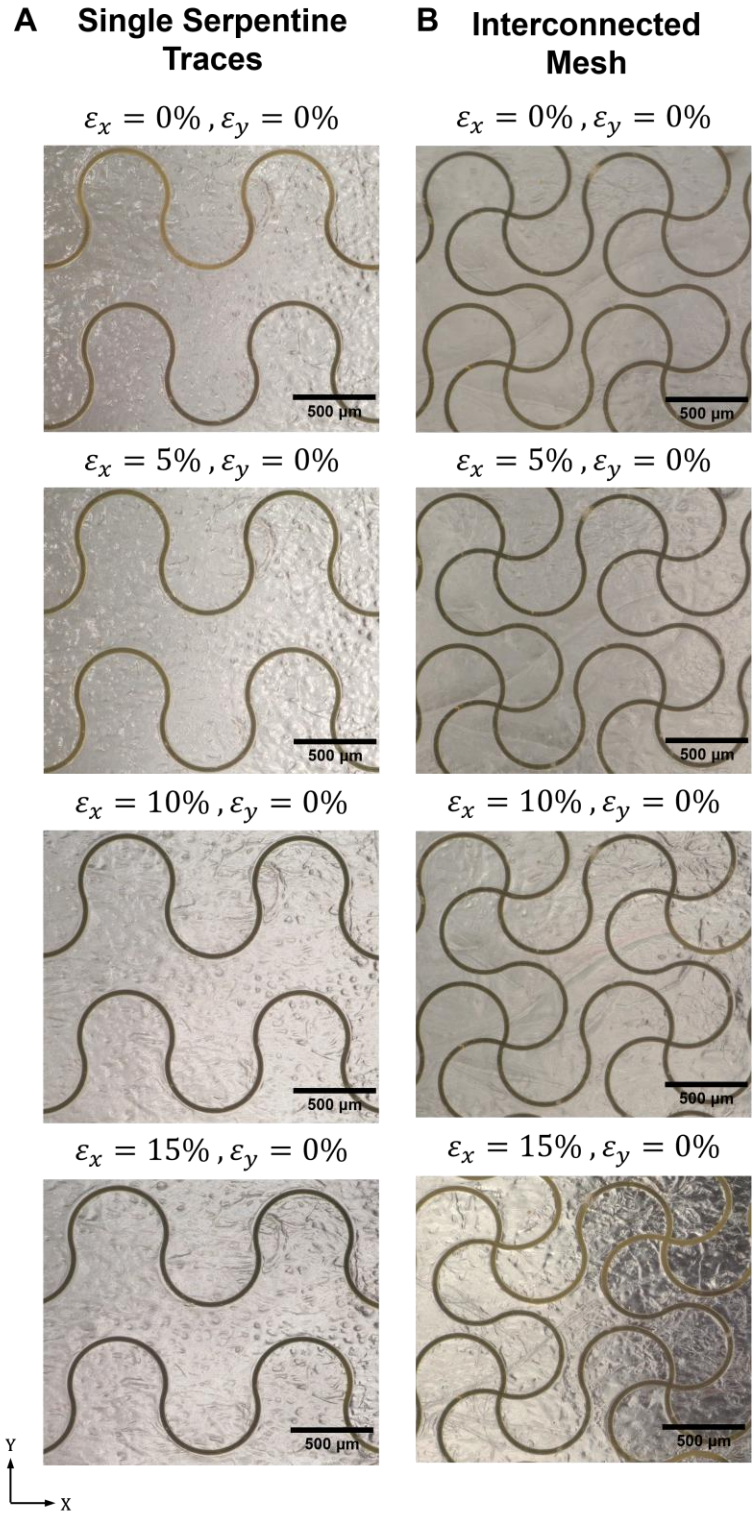

Figure A1. Experiments of deformation under uniaxial stretching. Optical images of the Single Serpentine Traces (A, left column) and Interconnected Mesh (B, right column) architectures at applied strains of 0%, 5%, 10%, and 15%. Scale bars: 500 µm.

REFERENCES

Abrego, A.M., Khan, W., Wright, C.E., Islam, M.R., Ghajar, M.H., Bai, X., Tandon, N., Seymour, J.P., 2023. Sensing local field potentials with a directional and scalable depth electrode array. J. Neural Eng. 20, 016041. https://doi.org/10.1088/1741-2552/acb230

Al Abed, A., Amatoury, J., Khraiche, M., 2022. Finite Element Modeling of Magnitude and Location of Brain Micromotion Induced Strain for Intracortical Implants. Front. Neurosci. 15. https://doi.org/10.3389/fnins.2021.727715

Bazargan-Hejazi, S., Dehghan, K., Edwards, C., Mohammadi, N., Attar, S., Sahraian, M.A., Eskandarieh, S., 2020. The health burden of non-communicable neurological disorders in the USA between 1990 and 2017. Brain Commun. 2. https://doi.org/10.1093/braincomms/fcaa097

Chung, H.U., Kim, B.H., Lee, J.Y., Lee, J., Xie, Z., Ibler, E.M., Lee, K., Banks, A., Jeong, J.Y., Kim, Jongwon, Ogle, C., Grande, D., Yu, Y., Jang, H., Assem, P., Ryu, D., Kwak, J.W., Namkoong, M., Park, J. Bin, Lee, Y., Kim, D.H., Ryu, A., Jeong, J., You, K., Ji, B., Liu, Z., Huo, Q., Feng, X., Deng, Y., Xu, Y., Jang, K.-I., Kim, Jeonghyun, Zhang, Y., Ghaffari, R., Rand, C.M., Schau, M., Hamvas, A., Weese-Mayer, D.E., Huang, Y., Lee, S.M., Lee, C.H., Shanbhag, N.R., Paller, A.S., Xu, S., Rogers, J.A., 2019. Binodal, wireless epidermal electronic systems with in-sensor analytics for neonatal intensive care. Science (1979). 363. https://doi.org/10.1126/science.aau0780

Chung, H.U., Rwei, A.Y., Hourlier-Fargette, A., Xu, S., Lee, K., Dunne, E.C., Xie, Z., Liu, C., Carlini, A., Kim, D.H., Ryu, D., Kulikova, E., Cao, J., Odland, I.C., Fields, K.B., Hopkins, B., Banks, A., Ogle, C., Grande, D., Park, J. Bin, Kim, Jongwon, Irie, M., Jang, H., Lee, J., Park, Y., Kim, Jungwoo, Jo, H.H., Hahm, H., Avila, R., Xu, Y., Namkoong, M., Kwak, J.W., Suen, E., Paulus, M.A., Kim, R.J., Parsons, B. V., Human, K.A., Kim, S.S., Patel, M., Reuther, W., Kim, H.S., Lee, S.H., Leedle, J.D., Yun, Y., Rigali, S., Son, T., Jung, I., Arafa, H., Soundararajan, V.R., Ollech, A., Shukla, A., Bradley, A., Schau, M., Rand, C.M., Marsillio, L.E., Harris, Z.L., Huang, Y., Hamvas, A., Paller, A.S., Weese-Mayer, D.E., Lee, J.Y., Rogers, J.A., 2020. Skin-interfaced biosensors for advanced wireless physiological monitoring in neonatal and pediatric intensive-care units. Nat. Med. 26, 418–429. https://doi.org/10.1038/s41591-020-0792-9

Coimbatore Balram, K., Westly, D.A., Davanco, M.I., Grutter, K.E., Li, Q., Michels, T., Ray, C.H., Kasica, R.J., Wallin, C.B., Gilbert, I.J., Bryce, B.A., Simelgor, G., Topolancik, J., Lobontiu, N., Liu, Y., Neuzil, P., Svatos, V., Dill, K.A., Bertrand, N.A., Metzler, M., Lopez, G., Czaplewski, D., Ocola, L., Srinivasan, K.A., Stavis, S.M., Aksyuk, V.A., Liddle, J.A.A., Krylov, S., Ilic, R.R.;, 2016. The Nanolithography Toolbox. J. Res. Natl. Inst. Stand. Technol. 121, 464. https://doi.org/10.6028/jres.121.024

Fan, Z., Zhang, Y., Ma, Q., Zhang, F., Fu, H., Hwang, K.-C., Huang, Y., 2016a. A finite deformation model of planar serpentine interconnects for stretchable electronics. Int. J. Solids Struct. 91, 46–54. https://doi.org/10.1016/j.ijsolstr.2016.04.030

Fan, Z., Zhang, Y., Ma, Q., Zhang, F., Fu, H., Hwang, K.-C., Huang, Y., 2016b. A finite deformation model of planar serpentine interconnects for stretchable electronics. Int. J. Solids Struct. 91, 46–54. https://doi.org/10.1016/j.ijsolstr.2016.04.030

Fomani, A.A., Moradi, M., Assaf, S., Mansour, R.R., 2010. 3D microprobes for deep brain stimulation and recording, in: 2010 Annual International Conference of the IEEE Engineering in Medicine and Biology. IEEE, pp. 1808–1811. https://doi.org/10.1109/IEMBS.2010.5626410

Freitas, J.R., Pimenta, S., Santos, D.J., Esteves, B., Gomes, N.M., Correia, J.H., 2022. Flexible Neural Probe Fabrication Enhanced with a Low-Temperature Cured Polyimide and Platinum Electrodeposition. Sensors 22, 9674. https://doi.org/10.3390/s22249674

Guan, S., Wang, J., Gu, X., Zhao, Y., Hou, R., Fan, H., Zou, L., Gao, L., Du, M., Li, C., Fang, Y., 2019. Elastocapillary self-assembled neurotassels for stable neural activity recordings. Sci. Adv. 5. https://doi.org/10.1126/sciadv.aav2842

Hopcroft, M.A., Nix, W.D., Kenny, T.W., 2010. What is the Young's Modulus of Silicon? Journal of Microelectromechanical Systems 19, 229–238. https://doi.org/10.1109/JMEMS.2009.2039697

Jeon, W., Lee, J.M., Kim, Y., Lee, Y., Won, J., Lee, S., Son, W., Koo, Y.H., Hong, J., Gwac, H., Joo, J., Kim, S.J., Choi, C., Park, S., 2024. Structurally Aligned Multifunctional Neural Probe (SAMP) Using Forest-Drawn CNT Sheet onto Thermally Drawn Polymer Fiber for Long-Term In Vivo Operation. Advanced Materials 36. https://doi.org/10.1002/adma.202313625

Jun, J.J., Steinmetz, N.A., Siegle, J.H., Denman, D.J., Bauza, M., Barbarits, B., Lee, A.K., Anastassiou, C.A., Andrei, A., Aydın, Ç., Barbic, M., Blanche, T.J., Bonin, V., Couto, J., Dutta, B., Gratiy, S.L., Gutnisky, D.A., Häusser, M., Karsh, B., Ledochowitsch, P., Lopez, C.M., Mitelut, C., Musa, S., Okun, M., Pachitariu, M., Putzeys, J., Rich, P.D., Rossant, C., Sun, W., Svoboda, K., Carandini, M., Harris, K.D., Koch, C., O'Keefe,

J., Harris, T.D., 2017. Fully integrated silicon probes for high-density recording of neural activity. Nature 551, 232–236. https://doi.org/10.1038/nature24636
Kim, J.-H., Nizami, A., Hwangbo, Y., Jang, B., Lee, H.-J., Woo, C.-S., Hyun, S., Kim, T.-S., 2013. Tensile testing of ultra-thin films on water surface. Nat. Commun. 4, 2520. https://doi.org/10.1038/ncomms3520
Kozai, T.D.Y., Catt, K., Li, X., Gugel, Z. V., Olafsson, V.T., Vazquez, A.L., Cui, X.T., 2015. Mechanical failure modes of chronically implanted planar silicon-based neural probes for laminar recording. Biomaterials 37, 25–39. https://doi.org/10.1016/j.biomaterials.2014.10.040
Kullmann, A., Akberali, F., Van Gompel, J.J., McGovern, R.A., Marsh, W.R., Kridner, D., Diaz-Botia, C.A., Park, M.C., 2024. Implantation accuracy of novel polyimide stereotactic electroencephalographic depth electrodes—a human cadaveric study. Front. Med. Technol. 6. https://doi.org/10.3389/fmedt.2024.1320762
Lacour, S.P., Courtine, G., Guck, J., 2016. Materials and technologies for soft implantable neuroprostheses. Nat. Rev. Mater. 1, 16063. https://doi.org/10.1038/natrevmats.2016.63
Li, M., Jiang, C., Zhang, Yuyan, Lin, Y., Zhang, Z., Liang, M., Zhang, Yupei, Fan, Z., Zhang, Yuwu, 2026. Impact dynamics of three-dimensional horseshoe microstructure lattice under indentation deformation. Int. J. Solids Struct. 334, 113965. https://doi.org/10.1016/j.ijsolstr.2026.113965
Liu, Y., Liu, J., Chen, S., Lei, T., Kim, Y., Niu, S., Wang, H., Wang, X., Foudeh, A.M., Tok, J.B.-H., Bao, Z., 2019. Soft and elastic hydrogel-based microelectronics for localized low-voltage neuromodulation. Nat. Biomed. Eng. 3, 58–68. https://doi.org/10.1038/s41551-018-0335-6
Luan, L., Wei, X., Zhao, Z., Siegel, J.J., Potnis, O., Tuppen, C.A., Lin, S., Kazmi, S., Fowler, R.A., Holloway, S., Dunn, A.K., Chitwood, R.A., Xie, C., 2017. Ultraflexible nanoelectronic probes form reliable, glial scar–free neural integration. Sci. Adv. 3. https://doi.org/10.1126/sciadv.1601966
Ma, Q., Cheng, H., Jang, K.-I., Luan, H., Hwang, K.-C., Rogers, J.A., Huang, Y., Zhang, Y., 2016. A nonlinear mechanics model of bio-inspired hierarchical lattice materials consisting of horseshoe microstructures. J. Mech. Phys. Solids 90, 179–202. https://doi.org/10.1016/j.jmps.2016.02.012
McGlynn, E., Walton, F., Das, R., Heidari, H., 2022. Neural microprobe modelling and microfabrication for improved implantation and mechanical failure mitigation. Philosophical Transactions of the Royal Society A: Mathematical, Physical and Engineering Sciences 380. https://doi.org/10.1098/rsta.2021.0007
Menghani, R.R., Avila, R., 2025. Functional criteria for substrates in soft and stretchable bioelectronic systems. npj Soft Matter 1, 11. https://doi.org/10.1038/s44431-025-00012-7
Nguyen, J.K., Park, D.J., Skousen, J.L., Hess-Dunning, A.E., Tyler, D.J., Rowan, S.J., Weder, C., Capadona, J.R., 2014. Mechanically-compliant intracortical implants reduce the neuroinflammatory response. J. Neural Eng. 11, 056014. https://doi.org/10.1088/1741-2560/11/5/056014
Pan, T., Pharr, M., Ma, Y., Ning, R., Yan, Z., Xu, R., Feng, X., Huang, Y., Rogers, J.A., 2017a. Experimental and Theoretical Studies of Serpentine Interconnects on Ultrathin Elastomers for Stretchable Electronics. Adv. Funct. Mater. 27. https://doi.org/10.1002/adfm.201702589
Pan, T., Pharr, M., Ma, Y., Ning, R., Yan, Z., Xu, R., Feng, X., Huang, Y., Rogers, J.A., 2017b. Experimental and Theoretical Studies of Serpentine Interconnects on Ultrathin Elastomers for Stretchable Electronics. Adv. Funct. Mater. 27. https://doi.org/10.1002/adfm.201702589
Park, S. Il, Brenner, D.S., Shin, G., Morgan, C.D., Copits, B.A., Chung, H.U., Pullen, M.Y., Noh, K.N., Davidson, S., Oh, S.J., Yoon, J., Jang, K.-I., Samineni, V.K., Norman, M., Grajales-Reyes, J.G., Vogt, S.K., Sundaram, S.S., Wilson, K.M., Ha, J.S., Xu, R., Pan, T., Kim, T., Huang, Y., Montana, M.C., Golden, J.P., Bruchas, M.R., Gereau, R.W., Rogers, J.A., 2015. Soft, stretchable, fully implantable miniaturized optoelectronic systems for wireless optogenetics. Nat. Biotechnol. 33, 1280–1286. https://doi.org/10.1038/nbt.3415
Pimenta, S., Freitas, J.R., Correia, J.H., 2024. Flexible neural probes: a review of the current advantages, drawbacks, and future demands. J. Zhejiang Univ. Sci. B 25, 153–167. https://doi.org/10.1631/jzus.B2300337
Pothof, F., Bonini, L., Lanzilotto, M., Livi, A., Fogassi, L., Orban, G.A., Paul, O., Ruther, P., 2016a. Chronic neural probe for simultaneous recording of single-unit, multi-unit, and local field potential activity from multiple brain sites. J. Neural Eng. 13, 046006. https://doi.org/10.1088/1741-2560/13/4/046006
Pothof, F., Bonini, L., Lanzilotto, M., Livi, A., Fogassi, L., Orban, G.A., Paul, O., Ruther, P., 2016b. Chronic neural probe for simultaneous recording of single-unit, multi-unit, and local field potential activity from multiple brain sites. J. Neural Eng. 13, 046006. https://doi.org/10.1088/1741-2560/13/4/046006
Qiang, Y., Gu, W., Jang, D., Shin, Y., Shi, D., Seo, K.J., Li, G., Vinnikova, S., Wu, S., Iyer, A., Artoni, P., Ryu, J., Bai, T., Dhawan, V., Medalla, M., Rosene, D.L., Moore, T.L., Koppes, A.N., Koppes, R., Liou, J., Chandrasekaran, C., Cui, X.T., Wang, S., Fang, H., 2025. Monolithic three-dimensional neural probes from

deterministic rolling of soft electronics. Nat. Electron. 8, 721–737. https://doi.org/10.1038/s41928-025-01431-0
Rogers, J.A., Someya, T., Huang, Y., 2010. Materials and Mechanics for Stretchable Electronics. Science (1979). 327, 1603–1607. https://doi.org/10.1126/science.1182383
Russo, S., Ranzani, T., Walsh, C.J., Wood, R.J., 2017. An Additive Millimeter-Scale Fabrication Method for Soft Biocompatible Actuators and Sensors. Adv. Mater. Technol. 2. https://doi.org/10.1002/admt.201700135
Salatino, J.W., Ludwig, K.A., Kozai, T.D.Y., Purcell, E.K., 2017. Glial responses to implanted electrodes in the brain. Nat. Biomed. Eng. 1, 862–877. https://doi.org/10.1038/s41551-017-0154-1
Savya, S.P., Li, F., Lam, S., Wellman, S.M., Stieger, K.C., Chen, K., Eles, J.R., Kozai, T.D.Y., 2022. In vivo spatiotemporal dynamics of astrocyte reactivity following neural electrode implantation. Biomaterials 289, 121784. https://doi.org/10.1016/j.biomaterials.2022.121784
Schulte, J., Ashouri, D., Stieglitz, T., 2024. The Longevity of Neural Interfaces—Mechanical Oscillation of Thin Film Metal-Based Neural Electrodes Determine Stability During Electrical Stimulation. Adv. Funct. Mater. 34. https://doi.org/10.1002/adfm.202310130
Sharafkhani, N., Kouzani, A.Z., Adams, S.D., Long, J.M., Lissorgues, G., Rousseau, L., Orwa, J.O., 2022a. Neural tissue-microelectrode interaction: Brain micromotion, electrical impedance, and flexible microelectrode insertion. J. Neurosci. Methods 365, 109388. https://doi.org/10.1016/j.jneumeth.2021.109388
Sharafkhani, N., Kouzani, A.Z., Adams, S.D., Long, J.M., Lissorgues, G., Rousseau, L., Orwa, J.O., 2022b. Neural tissue-microelectrode interaction: Brain micromotion, electrical impedance, and flexible microelectrode insertion. J. Neurosci. Methods 365, 109388. https://doi.org/10.1016/j.jneumeth.2021.109388
Sharon, A., Jankowski, M.M., Shmoel, N., Erez, H., Spira, M.E., 2021. Inflammatory Foreign Body Response Induced by Neuro-Implants in Rat Cortices Depleted of Resident Microglia by a CSF1R Inhibitor and Its Implications. Front. Neurosci. 15. https://doi.org/10.3389/fnins.2021.646914
Sim, K., Li, Y., Song, J., Yu, C., 2019. Stretchable Electronics: Biaxially Stretchable Ultrathin Si Enabled by Serpentine Structures on Prestrained Elastomers (Adv. Mater. Technol. 1/2019). Adv. Mater. Technol. 4. https://doi.org/10.1002/admt.201970003
Singh, S., Lo, M.-C., Damodaran, V., Kaplan, H., Kohn, J., Zahn, J., Shreiber, D., 2016. Modeling the Insertion Mechanics of Flexible Neural Probes Coated with Sacrificial Polymers for Optimizing Probe Design. Sensors 16, 330. https://doi.org/10.3390/s16030330
Sridharan, A., Nguyen, J.K., Capadona, J.R., Muthuswamy, J., 2015. Compliant intracortical implants reduce strains and strain rates in brain tissue in vivo. J. Neural Eng. 12, 036002. https://doi.org/10.1088/1741-2560/12/3/036002
Sridharan, A., Rajan, S.D., Muthuswamy, J., 2013a. Long-term changes in the material properties of brain tissue at the implant–tissue interface. J. Neural Eng. 10, 066001. https://doi.org/10.1088/1741-2560/10/6/066001
Sridharan, A., Rajan, S.D., Muthuswamy, J., 2013b. Long-term changes in the material properties of brain tissue at the implant–tissue interface. J. Neural Eng. 10, 066001. https://doi.org/10.1088/1741-2560/10/6/066001
Steinmetz, J.D., Seeher, K.M. et al., 2024. Global, regional, and national burden of disorders affecting the nervous system, 1990–2021: a systematic analysis for the Global Burden of Disease Study 2021. Lancet Neurol. 23, 344–381. https://doi.org/10.1016/S1474-4422(24)00038-3
Subbaroyan, J., Martin, D.C., Kipke, D.R., 2005. A finite-element model of the mechanical effects of implantable microelectrodes in the cerebral cortex. J. Neural Eng. 2, 103–113. https://doi.org/10.1088/1741-2560/2/4/006
Wang, L., Zhang, Chenrui, Hao, Z., Yao, S., Bai, L., Oliveira, J.M., Wang, P., Zhang, K., Zhang, Chen, He, J., Reis, R.L., Li, D., 2025a. Bioaugmented design and functional evaluation of low damage implantable array electrodes. Bioact. Mater. 47, 18–31. https://doi.org/10.1016/j.bioactmat.2024.12.033
Wang, L., Zhang, Chenrui, Hao, Z., Yao, S., Bai, L., Oliveira, J.M., Wang, P., Zhang, K., Zhang, Chen, He, J., Reis, R.L., Li, D., 2025b. Bioaugmented design and functional evaluation of low damage implantable array electrodes. Bioact. Mater. 47, 18–31. https://doi.org/10.1016/j.bioactmat.2024.12.033
Wang, M.-H., Nikaido, K., Kim, Y., Ji, B.-W., Tian, H.-C., Kang, X.-Y., Yang, C.-S., Yang, B., Chen, X., Wang, X.-L., Zhang, Y., Liu, J.-Q., 2017. Flexible cylindrical neural probe with graphene enhanced conductive polymer for multi-mode BCI applications, in: 2017 IEEE 30th International Conference on Micro Electro Mechanical Systems (MEMS). IEEE, pp. 502–505. https://doi.org/10.1109/MEMSYS.2017.7863453
Widlund, T., Yang, S., Hsu, Y.-Y., Lu, N., 2014. Stretchability and compliance of freestanding serpentine-shaped ribbons. Int. J. Solids Struct. 51, 4026–4037. https://doi.org/10.1016/j.ijsolstr.2014.07.025

Xie, Z., Ji, B., Huo, Q., 2018. Mechanics Design of Stretchable Near Field Communication Antenna With Serpentine Wires. J. Appl. Mech. 85. https://doi.org/10.1115/1.4039102

Ye, C., Stewart, B.G., Sitaraman, S.K., 2020. Stretchability of Serpentine Interconnect on Polymer Substrate for Flexible Electronics: A Geometry and Material Sensitivity Analysis, in: 2020 IEEE 70th Electronic Components and Technology Conference (ECTC). IEEE, pp. 1533–1541. https://doi.org/10.1109/ECTC32862.2020.00241

Zhang, L., Wang, S., Xia, J., Li, B., Zhang, S., Luo, J., Zhang, F., Zheng, T., Pan, G., Hasan, T., Yu, Y., Ding, G., Jin, H., Yang, Z., Dong, S., 2025. Monolithic multimodal neural probes for sustained stimulation and long-term neural recording. Sci. Adv. 11. https://doi.org/10.1126/sciadv.adu1753

Zhang, Y., Fu, H., Su, Y., Xu, S., Cheng, H., Fan, J.A., Hwang, K.-C., Rogers, J.A., Huang, Y., 2013a. Mechanics of ultra-stretchable self-similar serpentine interconnects. Acta Mater. 61, 7816–7827. https://doi.org/10.1016/j.actamat.2013.09.020

Zhang, Y., Fu, H., Su, Y., Xu, S., Cheng, H., Fan, J.A., Hwang, K.-C., Rogers, J.A., Huang, Y., 2013b. Mechanics of ultra-stretchable self-similar serpentine interconnects. Acta Mater. 61, 7816–7827. https://doi.org/10.1016/j.actamat.2013.09.020

Zhang, Y., Fu, H., Su, Y., Xu, S., Cheng, H., Fan, J.A., Hwang, K.-C., Rogers, J.A., Huang, Y., 2013c. Mechanics of ultra-stretchable self-similar serpentine interconnects. Acta Mater. 61, 7816–7827. https://doi.org/10.1016/j.actamat.2013.09.020

Zhang, Y., Xu, S., Fu, H., Lee, J., Su, J., Hwang, K.-C., Rogers, J.A., Huang, Y., 2013d. Buckling in serpentine microstructures and applications in elastomer-supported ultra-stretchable electronics with high areal coverage. Soft Matter 9, 8062. https://doi.org/10.1039/c3sm51360b

Figure Captions

Figure 1. Design and fabrication of stretchable neural probe designs. (**A**) Schematic illustration of the intended neural probe application and the two investigated interconnect topologies: Single Serpentine Traces and Interconnected Mesh (Created in BioRender. https://BioRender.com/zp3he8z). (**B**) Cross-sectional architecture of the multilayer system comprising Au interconnects encapsulated within polyimide (PI), embedded in an Ecoflex substrate, and supported by a NuSil backing layer. (**C,D**) Geometric definitions of the serpentine unit cell, characterized by trace width w, arc radius r, and offset angle θ, for the Single Serpentine Traces and Interconnected Mesh architectures, respectively, along with the corresponding finite-element geometries used for mechanical analysis. (**E,F**) Optical micrographs of fabricated Single Serpentine Traces and Interconnected Mesh samples. Scale bars: 500 μm

Figure 2. Wrapping mechanics and conformability of the neural probe architecture. (Left) Optical image of the interconnects in a cylindrical architecture wrapped around a 800 μm stainless steel guidewire demonstrating conformal integration onto a small-radius cylindrical substrate (scale bar: 2.5 mm) pictured next to PMT SEEG, the current clinical standard. Arrows indicate the Au serpentine interconnects distributed along the electrode shaft. **(Right)** Enlarged view of the mesh electrode highlighting the serpentine interconnect geometry that enables conformal wrapping (scale bar: 500 μm)

Figure 3. **Stress–strain relation adopted for the Au interconnects**. The initial linear regime defines the elastic response, while subsequent strain hardening governs the post-yield behavior. The yield point $(\varepsilon_{yield}, \sigma_{yield})$ and fracture point $(\varepsilon_f, \sigma_f)$ provide the critical criteria for assessing the onset of plasticity and failure throughout the deformation analyses.

Figure 4. Geometry and loading sequence for conformal wrapping. (**A**) A planar serpentine mesh is transformed into a cylindrical configuration through prescribed end rotations about the probe axis. (**B**) Representative configurations at $\varphi = 0$, $\pi/2$, $3\pi/4$, and π illustrate the progressive development of curvature and contact during integration onto the cylindrical substrate.

Figure 5. Uniaxial stretching mechanics of the Single Serpentine Traces and Interconnected Mesh architectures. **(A,B)** Deformed configurations and von Mises stress distributions in the Au interconnects at $\varepsilon_x = 30\%$, with enlarged views of representative serpentine unit cells. The paths L_{AB} and W_{CD} define the directions used for stress analysis. **(C,D)** Experimental images of the corresponding stretched configurations. **(E,F)** Stress profiles along L_{AB} and **(G,H)** stress profiles along W_{CD} for applied strains ranging from 5% to 30%. Dashed and dotted horizontal lines indicate the fracture and yield stresses of Au, respectively.

Figure 6. Loading-direction dependence of stress localization in stretchable neural probe architectures. **(A–F)** Stress distributions in the Au interconnects and substrate for uniaxial x-direction stretching, uniaxial y-direction stretching, and equal biaxial stretching at $\varepsilon_0 = 10\%$. Insets highlight representative serpentine unit cells and the associated stress concentrations. **(G,H)** Maximum interconnect stress as a function of applied strain for the three loading modes. The dashed horizontal line denotes the Au yield stress, defining the onset of plastic deformation.

Figure 7. Mechanics of conformal wrapping onto cylindrical neural probes. (A,B) Interconnect stress distributions for the Single Serpentine Traces and Interconnected Mesh architectures wrapped around a probe of radius $R = 0.4$mm. **(C,D)** Experimental images of the corresponding wrapped configurations. **(E)** Mean, maximum, and minimum interconnect stresses as a function of cylinder radius (R = 0.4 - 0.7 mm) for both architectures. Bars denote the max/min range of the stress distribution within the Au interconnects. The horizontal dashed line indicates the Au yield stress.

Figure 8. Bending mechanics of conformally wrapped neural probes. **(A)** Cantilever bending configuration and definition of the normalized probe position a/l. **(B)** Representative deformation sequence under increasing tip displacement. **(C,D)** Stress distribution in the Au interconnects for the deformed configurations of the Single Serpentine Traces and Interconnected Mesh architectures at $a/l = 0.5$. **(E,F)** Maximum interconnect stress as a function of tip displacement for different probe locations. The slope $m = \Delta\sigma/\Delta\delta$ characterizes the sensitivity of the interconnect stress to bending-induced curvature.

Figure 9. Relative contributions of wrapping and bending to stress development in conformal neural probes. **(A)** Single Serpentine Traces. **(B)** Interconnected Mesh. Maximum interconnect stresses are shown for the wrapped state and after bending at different normalized probe locations. The comparison isolates the incremental stress associated with bending-induced curvature from that generated during conformal wrapping.